Defining Cellular Diversity at the Swine Maternal-Fetal Interface Using Spatial Transcriptomics and Organoids

Cole R. McCutcheon[1], Allyson Caldwell[1], Liheng (Henry) Yang[1], Elisa Crisci[2], J. Alex Pasternak[3], Carolyn B. Coyne[1,4*]

1) Duke University School of Medicine, Department of Integrative Immunobiology, Durham, NC
2) Department of Population Health and Pathobiology, College of Veterinary Medicine, North Carolina State University, Raleigh, NC
3) Department of Animal Sciences, Purdue University, West Lafayette, IN
4) Duke Human Vaccine Institute, Durham, NC

*Address correspondence:
Carolyn Coyne, PhD
3130 Medical Sciences Research Building III
3 Genome Court
Durham, NC 27710
USA
carolyn.coyne@duke.edu

ABSTRACT

The placenta is a dynamic, embryo-derived organ essential for fetal growth and development. While all eutherian mammals have placentas composed of fetal-derived trophoblasts that mediate maternal-fetal exchange, their anatomical and histological structures vary across species due to evolutionary divergence. Despite the cellular heterogeneity of porcine trophoblasts *in vivo*, understanding the mechanisms driving porcine placental development has been limited by the lack of *in vitro* models replicating this heterogeneity. In this study, we derived swine trophoblast organoids (sTOs) from full-term porcine placentas, retaining key transcriptional signatures of *in vivo* trophoblasts. To identify conserved cell populations, we integrated Visium spatial transcriptomics from mid-gestation porcine placentas with single-cell transcriptomics from sTOs. Spatial transcriptomics revealed novel markers of the porcine uterus and placenta, enabling precise separation of histological structures at the maternal-fetal interface. The integration of tissue and sTO transcriptomics showed that sTOs spontaneously differentiate into distinct trophoblast populations, with conserved gene expression and cell communication programs. These findings demonstrate that sTOs recapitulate porcine placental trophoblast populations, offering a powerful model for advancing placentation research. Our work also provides a spatially resolved whole-transcriptome dataset of the porcine maternal-fetal interface, opening new avenues for discoveries in placental development, evolution, and health across mammals.

63 **INTRODUCTION**

64 The defining feature of eutherian mammals is the presence of the fetal derived placenta.
65 The placenta is critical for fetal growth due to its numerous functions ranging from nutrient
66 transfer[1,2], steroidogenesis[3], and immunological defense[4,5]. While these placental functions are
67 largely maintained across species, the placenta has repeatedly evolved via a combination of
68 convergent and divergent evolution resulting in variable placental morphologies across species[6,7].

69 Placental structure is commonly categorized by the tissue layers separating the maternal
70 and fetal vasculature[7,8]. In the most invasive placental type, termed hemochorial, the placenta
71 erodes the uterine epithelium and remodels the uterine vasculature resulting in the influx of
72 maternal blood which directly bathes the placental epithelial cells, termed trophoblasts [7]. This type
73 of placentation is observed in many species including humans and rodents. Conversely, porcine
74 placentae are considered the least invasive placental type, termed epitheliochorial. In this system
75 the uterine vasculature, stroma and epithelium remain intact due to a lack of invasion by the
76 trophoblast cells [7]. In this case, the primary contact point for the placenta is the uterine epithelium.
77 Critically, regardless of the placental type or structure, all gas and nutrient transfer must occur
78 across the trophoblast layer [9].

79 In humans, trophoblasts consist of several subpopulations[10,11]. The three primary classes
80 of trophoblasts include cytotrophoblasts (CTBs), extravillous trophoblasts (EVTs), and the
81 multinucleated syncytiotrophoblast (STB). CTBs represent the mononuclear, proliferative,
82 undifferentiated trophoblast population of the placenta[10] whereas EVTs are highly invasive,
83 immunosuppressive cells, that primarily serve to remodel the maternal spiral arteries[12-14].
84 Conversely, the STB is a terminally differentiated multinuclear trophoblast population that covers
85 the entire surface of the chorionic villi. They serve dual roles as both a barrier to infection and a
86 critical site layer for nutrient and gas transfer[15,16].

87 Unlike human trophoblasts, which have been heavily characterized and subtyped, the
88 properties and subpopulations of swine trophoblasts are comparatively unknown, but several lines

89 of evidence suggest that subpopulations exist. First, the point of contact between the fetal
90 trophoblasts and uterine epithelium, termed the maternal-fetal interface, is extensively folded to
91 enhance placental surface area[17]. Along these folds, it has been reported that aquaporins [18] and
92 various transporters vary in expression[19], suggesting that trophoblast polarization along these
93 folds occurs. Second, the porcine placenta contains areolae, a cluster of specialized, columnar
94 trophoblast cells that sit atop uterine glands and facilitate the transfer of uterine gland secretions
95 to the developing fetus[20]. It is known that areolar trophoblasts are primed to uptake uteroferrin
96 compared to other trophoblasts[21] and express specific markers, such as cathepsin L1 (CTSL)[22],
97 suggesting a unique pattern of differentiation.

98 A major hurdle to furthering our understanding of porcine placentation is the lack of
99 suitable *in vitro* models. Limited access, coupled with high expense render *in vivo* and *ex vivo*
100 models challenging. While porcine trophoblast cell lines, such as PTr2[23,24], Jag-1[25], and pTR
101 cells[26] are available, these cells likely represent pre-implantation trophoblasts. Whether these cell
102 lines recapitulate later stages of placental development or the cellular heterogeneity observed *in*
103 *vivo* remains unclear.

104 In human and murine systems, organoids have proven to be a valuable tool for studying
105 complex biological systems in part because they can be cryopreserved, are scalable, and are
106 often tractable[27]. Furthermore, as organoids spontaneously differentiate into various cell
107 populations, they represent one of the most physiologically relevant *in vitro* models[27]. We and
108 others have successfully derived trophoblast organoids from human and non-human primate
109 (NHP) placentas, demonstrating that they recapitulate the cellular heterogeneity and gene
110 expression patterns of the human and NHP placenta[28-32]. Because of the success of trophoblast
111 organoid models, we sought to develop a similar model of the swine placenta. Here, we show the
112 derivation of swine trophoblast organoids (sTOs) from full-term placental tissue. Our data
113 demonstrate that sTO can be expanded, passaged, and cryopreserved and recapitulate the
114 expression of canonical markers of the swine placenta. Using Visium spatial transcriptomics of

115 mid-gestation swine placentas, we identified the gene signatures of diverse trophoblast
116 populations *in vivo* and identified novel maternal-fetal crosstalk pathways. By coupling spatial
117 transcriptomics of whole placentas with single-cell transcriptomics from sTO, we found that
118 organoids spontaneously differentiated into various trophoblast populations, accurately
119 replicating their gene signatures. Additionally, we identified gene changes along a differentiation
120 trajectory in sTOs, revealing signatures associated with the differentiation of distinct swine
121 trophoblast subpopulations. Taken together, these data demonstrate that sTO provide an
122 accurate and comprehensive model of the swine placenta, offering a powerful tool for advancing
123 studies of porcine placentation and reproductive biology *in vitro*.
124

125 **RESULTS**

126 **Derivation and long-term expansion of Swine Trophoblast Organoids**

127 To derive swine trophoblast organoids (sTOs), we collected full-term swine placenta tissue and
128 applied a similar two-step enzymatic digestion protocol used previously for the derivation of
129 human TOs (hTOs)[29] (**Figure 1A**). Isolated stem/progenitor cells were resuspended in Matrigel
130 and allowed to self-organize over a period of 7-10 days until spherical structures, reminiscent of
131 hTOs, were observed via brightfield microscopy (**Figure 1B, 1C**). Organoids were isolated from
132 initial wells by picking out single organoids, dissociated them, and then passaging using a
133 combination of enzymatic and mechanical dissociation. sTO growth was robust and scalable, with
134 an average propagation interval of 5-7 days. Unlike hTOs, which develop with "mini-cavities" at
135 their centers[28], sTOs exhibited a denser structure with no visible central cavities, which may reflect
136 species-specific differences in tissue architecture and cellular organization (**Figure 1C, 1D**).
137 Similar to hTOs, sTOs could be continuously passaged with no apparent phenotypic changes
138 (e.g., organoid size, morphology, growth kinetics) and can be cryopreserved and revived. We
139 successfully derived sTOs from five unique swine placentas with 100% success across all tissues
140 collected.

141 A limitation of hTOs is their inverted polarity when grown in Matrigel “domes”, resulting in
142 an inward-facing STB that does not accurately mimic the cellular polarity of the human placenta
143 *in vivo*[28]. To define the cellular orientation of sTOs, we performed immunostaining with the tight
144 junction marker ZO-1, which localizes to the apical surface of swine trophoblasts *in vivo* [33]. We
145 found that sTOs expressed ZO-1, which localized to the inner surface of organoids when grown
146 in Matrigel (**Figure 1E**). We showed previously that hTOs cultured in suspension grow with more
147 physiologic polarity, with the STB on the outer surface[28]. Using a similar approach, we found that
148 sTOs also reversed their polarity when grown in suspension for approximately 48 hours and that
149 ZO-1 relocalized to the organoid outer surface (**Figure 1F**). sTOs grown in suspension also
150 displayed a more cystic morphology (**Figure 1G**). This suggests that the polarity of sTOs is easily
151 reversed, allowing for flexibility in experimental design.

152 To assess the ability of sTOs to recapitulate tissue-specific gene expression profiles, we
153 performed principal component analysis (PCA) on bulk RNA sequencing data from sTOs and
154 publicly available datasets of mid-gestation and full-term placental tissue as well as PTr2 cells,
155 which is a commonly used as *in vitro* model of swine trophoblasts. This approach allowed us to
156 compare the global transcriptional landscapes of organoids and their corresponding tissues,
157 identifying key patterns and similarities that indicate how closely sTOs mimic the native tissue
158 profile. We found that sTOs were more similar to placental tissue than PTr2 cells, which exhibited
159 a highly distinct expression pattern than both sTOs and placenta tissue (**Figure 1H**). sTOs also
160 expressed canonical markers of swine trophoblasts from placental tissue, whereas PTr2 cells did
161 not (**Figure 1I**). Using a previously established protocol for porcine sex determination which relies
162 on the expression of key Y-linked genes, we determined that sTO were derived from both male
163 and female placentae (**Figure 1J**)[34]. Together, these data indicate that sTO are composed of
164 fetal-derived swine trophoblasts.

165

166

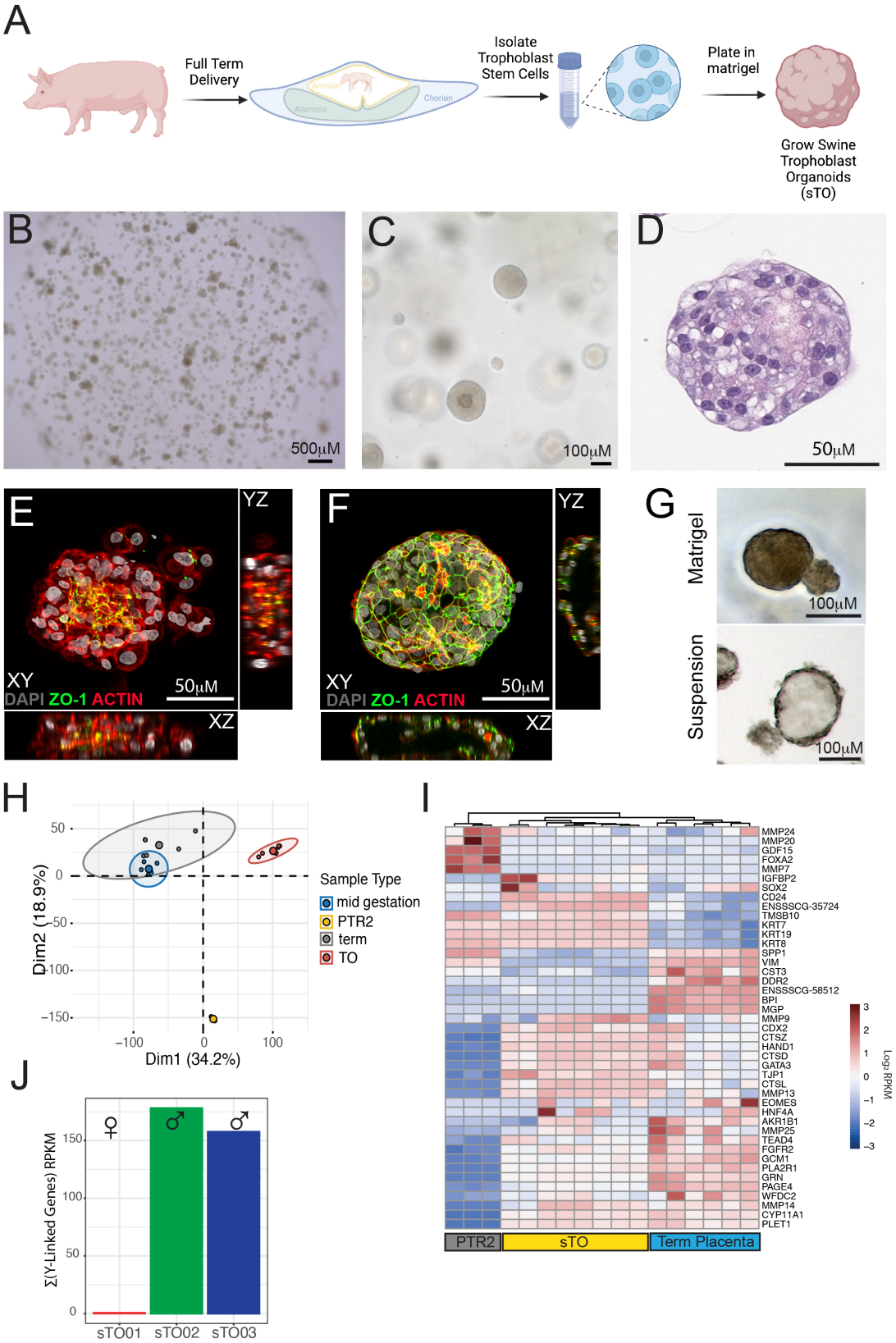
A
Full Term Delivery
Amnion
Allantois
Chorion
Isolate Trophoblast Stem Cells
Plate in matrigel
Grow Swine Trophoblast Organoids (sTO)
B
500μM
C
100μM
D
50μM
E
YZ
XY
DAPI ZO-1 ACTIN
50μM
XZ
F
YZ
XY
DAPI ZO-1 ACTIN
50μM
XZ
G
Matrigel
100μM
Suspension
100μM
H
Dim2 (18.9%)
Dim1 (34.2%)
Sample Type
mid gestation
PTR2
term
TO
I
MMP24
MMP20
GDF15
FOXA2
MMP7
IGFBP2
SOX2
CD24
ENSSSCG-35724
TMSB10
KRT7
KRT19
KRT8
SPP1
VIM
CST3
DDR2
ENSSSCG-58512
BPI
MGP
MMP9
CDX2
CTSZ
HAND1
CTSD
GATA3
TJP1
CTSL
MMP13
EOMES
HNF4A
AKR1B1
MMP25
TEAD4
FGFR2
GCM1
PLA2R1
GRN
PAGE4
WFDC2
MMP14
CYP11A1
PLET1
Log2 RPKM
PTR2
sTO
Term Placenta
J
Σ(Y-Linked Genes) RPKM
♀
♂
♂
sTO01
sTO02
sTO03

167

168

Figure 1: Establishment and validation of swine trophoblast organoids (sTO). A) Schematic of sTO derivation workflow. **B)** Representative low magnification brightfield image from a single well of sTO. **C)** High magnification brightfield image of sTO grown in Matrigel. **D)** Representative Hematoxylin and Eosin staining of a sectioned sTOs. **E)** Immunofluorescence microscopy image of sTO grown in Matrigel "domes". Apical marker ZO-1 is in green, DAPI in gray, and Actin in red. **F)** Immunofluorescence microscopy image of sTOs grown in suspension for 48 hours. Apical marker ZO-1 is in green, DAPI in gray, and Actin in red. **G)** Representative brightfield image of sTO grown in Matrigel "dome" (top) and suspension (bottom). **H)** PCA of bulk RNA-seq data from sTO, porcine trophoblast cell line (PTr2), as well as term and mid-gestation pig placentas. Points represent individual biological replicates, whereas circles denote 95% confidence intervals. **I)** Heatmap of known pig placentae markers expressed across PTr2 cells, sTOs, and term pig placentae. Individual columns indicate replicates. J.) Bar-plot showing the summation of RPKM for nine Y-linked genes across 3 individual sTO lines. sTO lines are denoted on the x-axis.

Single-cell Transcriptional Profiling Reveals Cellular Heterogeneity in sTOs

To determine whether sTOs differentiated into multiple trophoblast lineages, we next performed single-cell RNA-sequencing on three unique lines of sTOs. This analysis revealed five cell clusters (**Figure 2A**), with similar proportions across lines (**Figure 2B**). Canonical trophoblast markers including KRT7, KRT18, KRT8, ELF3, and FGFR2 were highly expressed in sTOs (**Figure 2C**) with low expression of the fibroblast markers VIM, PDGFRA, and COL1A1, indicating sTOs are a pure population of trophoblasts (**Figure 2D**). Cluster gene expression enrichment analysis revealed that trophoblast clusters were discernable by cluster-specific gene expression (**Figure 2E, Supplemental Table 1**). For example, cluster 0 was enriched with transcripts such as SOX5 and WNT6, cluster 1 had enriched expression of tight junction-associated genes OCLN and CLDN1, cluster 2 was marked by cell proliferation genes like TOP2A, cluster 3 showed high expression of inflammatory genes including CXCL8 and interferon-stimulated genes (ISGs), and cluster 4 exhibited elevated levels of COX enzymes (**Figure 2E**). Previous studies using *in situ* hybridization and antibody staining have identified markers of both swine interface trophoblasts and areolar trophoblasts[18,22,35]. While we observed expression of these markers within sTO cell populations, they did not fully segregate the trophoblast populations, ultimately limiting the utility of these markers to define the cellular identity of sTO-derived clusters (**Figure 2F**). Of note, we did observe that known pan-trophoblast markers such as CTSB and KRT18 were uniformly

expressed in sTOs suggesting that these various sTO cell populations are distinctive lineages rather than contaminating cell populations (**Figure 2G**). While this analysis identified several trophoblast populations in sTOs, the lack of a comprehensive marker list specific to the swine maternal-fetal interface made it difficult to definitively assign cellular identities to these clusters.

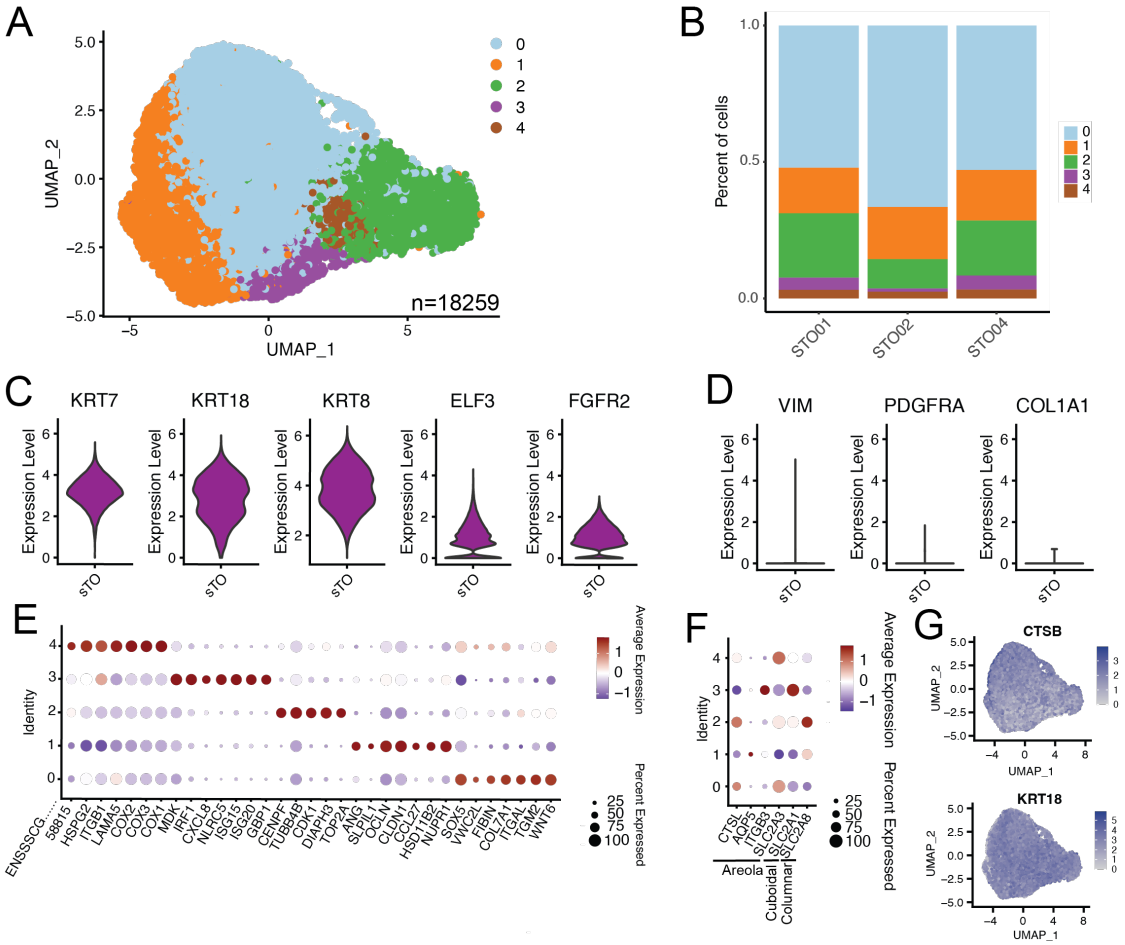

Figure 2: Single-cell transcriptomics of sTOs reveals cellular heterogeneity. A) UMAP from single cell transcriptomics of 3 independent lines of sTOs. **B)** Stacked bar-plot showing the relative proportions of various cell populations across three sTO lines. **C)** Violin plot showing the expression of canonical trophoblast markers in sTO single cell data. **D)** Violin plot showing the expression of canonical fibroblast markers in sTO single cell data. **E)** Dot-plot showing the top enrichment markers for various cell populations in sTOs. Color of dots denote average expression, whereas size represents percentage of cells in a cluster expressing the gene of interest. **F)** Dot-plot of canonical markers of various porcine trophoblast populations. Color of dots denote average expression, whereas size represents percentage of cells in a cluster expressing the gene of interest. **G)** Feature plot showing widespread expression of pan-trophoblast markers in sTOs.

218 **Visium-Based Spatial Transcriptomics Reveals Cellular Architecture at the Swine**
219 **Maternal-Fetal Interface**

220 To define the transcriptional signature of various cell populations comprising the porcine maternal-
221 fetal interface, we utilized Visium spatial transcriptomics, which allows for high-resolution spatial
222 mapping of gene expression. We applied this approach to mid-gestation maternal-fetal interfaces
223 (uterus with attached placenta) from four separate pregnancies (2 male and 2 female), enabling
224 the precise localization of gene expression patterns within the tissue architecture (**Figure 3A**).
225 Our analysis identified 10 distinct cell populations among the four placentae analyzed (**Figure**
226 **3B, Supplemental Figure 1A**). To assign cellular and regional identities to these clusters, we
227 utilized a combination of known marker expression (**Figure 3C**), histology (**Figure 3D**), and
228 cluster-specific gene enrichment analysis (**Supplemental Table 2**). Notably, the maternal and
229 fetal compartments were also discernable using this clustering technique (**Figure 3E,**
230 **Supplemental Figure 1B**). The maternal compartment was divided into six clusters: the
231 myometrium, represented by clusters 0 (Myo-1) and 6 (Myo-2); the endometrium, represented by
232 cluster 1 (Endo); blood and blood vessels, represented by clusters 7 (Blood) and 4 (Vasc); and
233 the uterine epithelium, represented by cluster 3 (UtEp) (**Figure 3D, 3F, Supplemental Figure**
234 **1C**). The fetal compartment was divided into four cell populations: the interface trophoblasts,
235 represented by cluster 5 (IntTroph); the areolae, represented by clusters 8 (Areola-1) and 9
236 (Areola-2); and the interstitium, represented by cluster 2 (Ist) (**Figure 3D, 3F, Supplemental**
237 **Figure 1C**). We observed some degree of sample-to-sample variability, which stemmed primarily
238 from differences in both cellular makeup and tissue structure between sections (**Figure 3G**).
239 Myometrium clusters were primarily defined by the expression of smooth muscle markers,
240 including SMTN, CNN1, ACTG2, MYL9, and MYLK. Blood vessels were characterized by the
241 expression of CLDN11 and CCL21, while blood cells were classified by high levels of ALAS2 and
242 HBM (**Figure 3C**). The endometrium was marked by elevated expression of SLPI and MEP1B,
243 both well-known to be expressed in this tissue (**Figure 3C**). Uterine epithelial cells expressed high

244 levels of established markers IGFBP2 and IGFBP3, whereas interface trophoblasts showed
245 elevated expression of pregnancy-stimulated genes (PSGs), PAGE4, PAG2L4, and HSD3B1
246 (**Figure 3C**). The interstitium cluster was defined by the expression of APOE, PEG10, DLK1, and
247 GPC3 (**Figure 3C**). Finally, the areola clusters were divided into two histologically and
248 transcriptionally distinct populations: Areola-1, characterized by high CTSL expression, and
249 Areola-2, with moderate CTSL expression. Areola-1 also expressed high levels of LIF and
250 MMP25, while Areola-2 was distinguished by elevated expression of LRP2, CYP11A1, and MMP7
251 (**Figure 3C, 3H**). Where Areola-2 displayed a structure that is continuous with the interface
252 trophoblasts, Areola-1 did not appear to be continuous with the interface trophoblasts (**Figure 3D,**
253 **3H, Supplemental Figure 1C**), suggesting these distinct structures may have different functions.

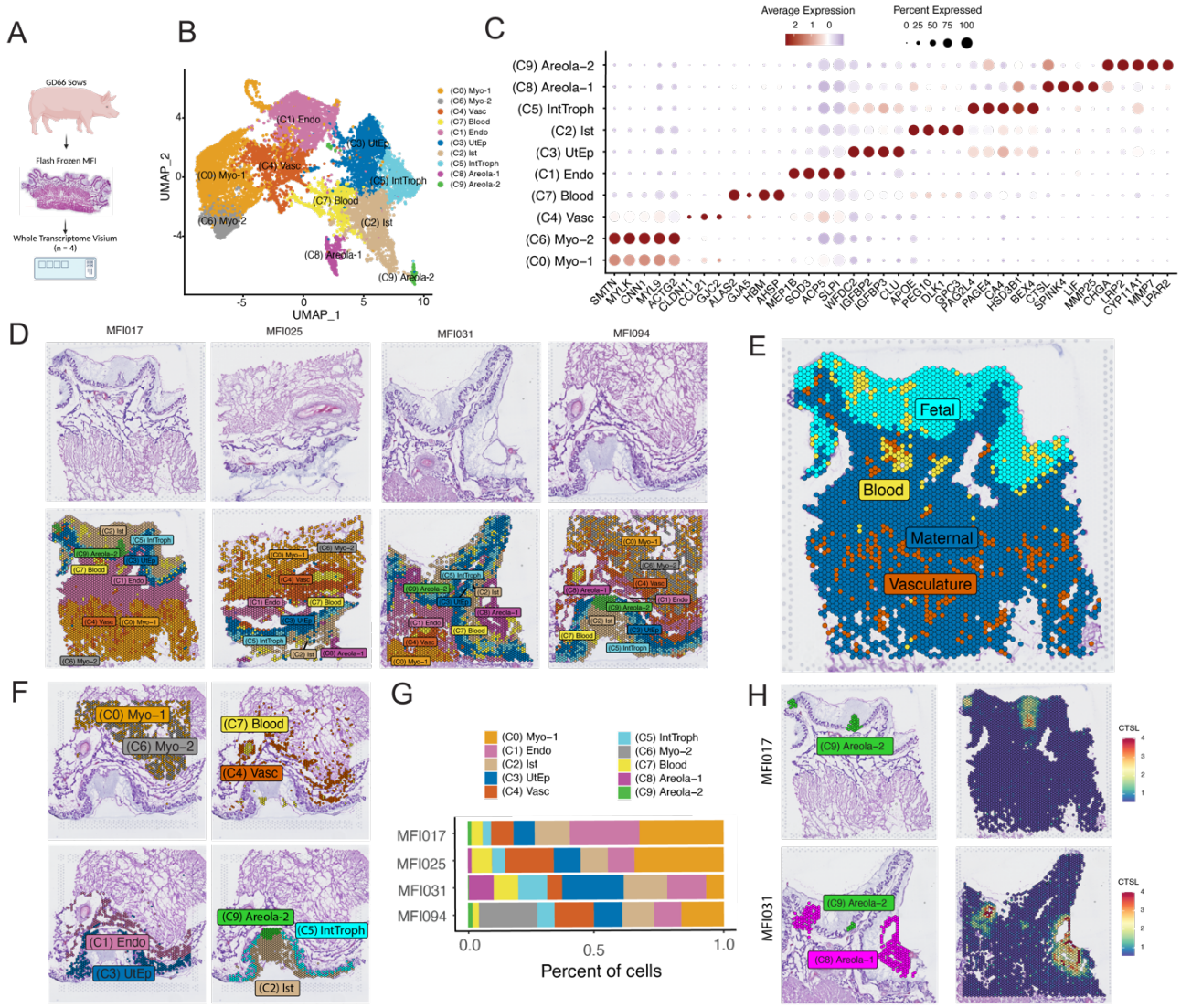

Figure 3: Spatial Transcriptomics Resolves Global Expression at the Porcine Maternal-Fetal Interface. A) Schematic of spatial transcriptomics workflow of gestational day 66 (GD66) maternal fetal interfaces (n = 4; 2 male and 2 female). **B)** UMAP showing 10 distinct populations obtained via spatial transcriptomics. **C)** Dot-plot of top markers for each cluster obtained via spatial transcriptomics. Color of dots denote average expression, whereas size represents percentage of cells in a cluster expressing the gene of interest. **D)** H&E staining of individual porcine maternal-fetal interface sections (top). Spatial DimPlot showing the histologic localization of UMAP cluster populations (bottom). Each image represents a separate maternal-fetal interface. **E)** Spatial Dim-plot showing separation of maternal and fetal compartments. Representative maternal-fetal Interface shown. **F)** Spatial Dim-Plot showing the histologic localization of UMAP individual cluster populations. Representative maternal-fetal Interface shown (MFI094). **G)** Stacked bar-plot showing the relative proportion of each cluster across individual maternal-fetal interfaces. **H)** Spatial DimPlot (Left panels) and Spatial Feature plots (Right panels) showing the localization of areola-1 and areola-2 structures (Left panels) and the expression of CTSL (right panels) within representative maternal-fetal interfaces.

271 **Defining Cellular Markers at the Swine Maternal-Fetal Interface Through Spatial**
272 **Transcriptomics**

273 Using the spatial transcriptomics dataset described above, we analyzed the cellular and molecular
274 landscape of the swine maternal-fetal interface to identify distinct markers associated with specific
275 cell types and regions. This approach enabled us to map the spatial distribution of key genes,
276 including those enriched in select trophoblast populations. To identify trophoblast specific
277 markers, we performed differential expression analysis between clusters containing trophoblasts,
278 (clusters 5, 8 and 9) and all other clusters. This analysis revealed both pan-trophoblast markers,
279 and markers of specific trophoblast populations (**Figure 4A, 4B, Supplemental Figure 2A-E**).
280 Specifically, the genes encoding cathepsin Z (CTSZ) and cathepsin B (CTSB) were highly
281 expressed in both interface trophoblasts as well as areolae trophoblasts, but only weakly
282 expressed elsewhere (**Figure 4A, 4B, Supplemental Figure 2A**). Similarly, the genes encoding
283 carbonic anhydrase 4 (CA4) and pregnancy associated glycoprotein L4 (PAG2L4) demarcated
284 interface trophoblasts (**Figure 4A, 4B, Supplemental Figure 2B**). Areolar trophoblasts
285 universally expressed CTSL (**Figure 3H, Supplemental Figure 2C**); however, areola-1
286 trophoblasts specifically expressed coiled coil domain containing 162 (CCDC162) and serine
287 peptidase inhibitor kazal type 4 (SPINK4) (**Figure 4A, 4B, Supplemental Figure 2E**).
288 Conversely, areola-2 trophoblasts were marked by an upregulation of matrix metalloprotease 7
289 (MMP7) and anterior gradient protein 2 homolog (AGR2) (**Figure 4A, 4B, Supplemental Figure**
290 **2D**). Notably, all of these highly specific markers were also detected within sTO, with varied
291 expression levels across clusters, suggesting some degree of differentiation across sTO cell
292 populations (**Figure 4C**). Although these markers partially resolved the clusters, their leaky
293 expression across multiple clusters limited our ability to accurately assign cellular identities.
294

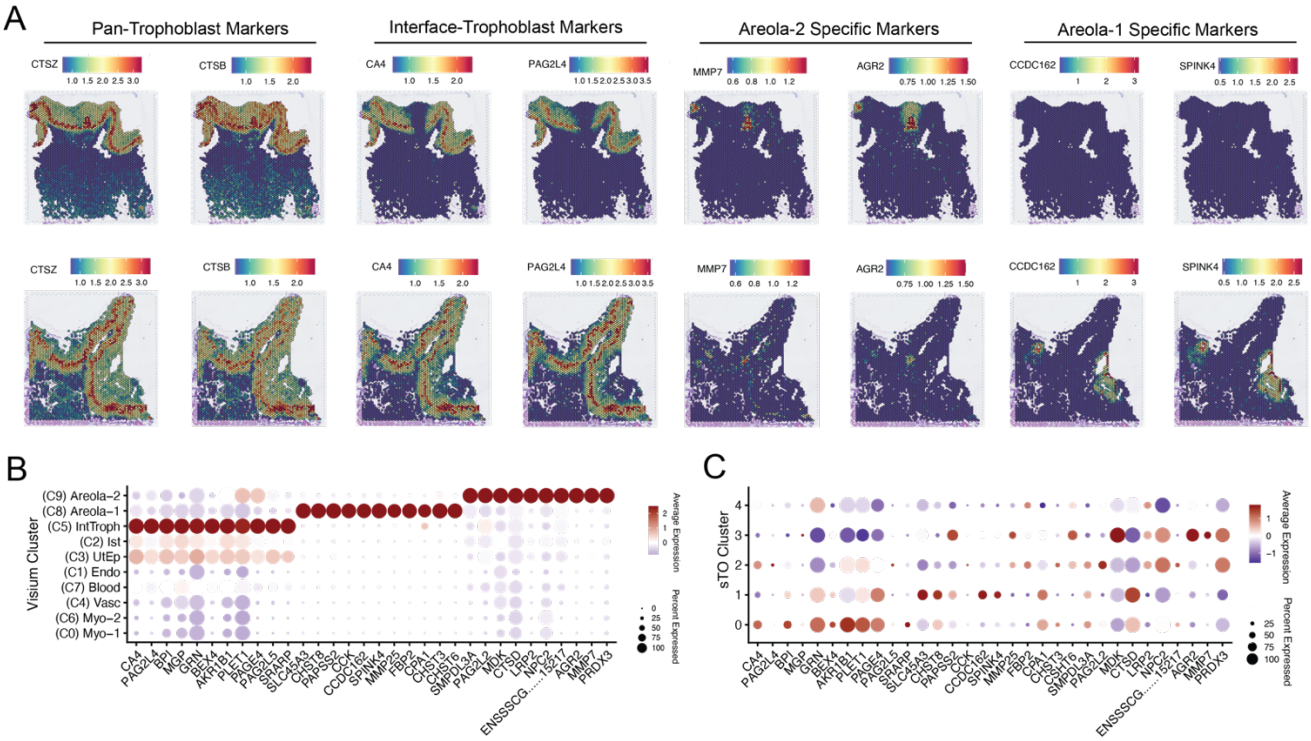

Figure 4: Spatial Transcriptomics Identifies Novel Trophoblast Specific Markers. A) Spatial FeaturePlots showing the localization of known or novel pan-trophoblast markers, interface-trophoblast markers, areola-2 and areola-1 specific markers. Two representative maternal-fetal interfaces are shown. **B)** DotPlot showing expanded markers of various trophoblast populations within the maternal-fetal interface. Color of dots denote average expression, whereas size represents percentage of cells in a cluster expressing the gene of interest. **C)** DotPlot showing the cluster specific expression of known and novel trophoblast markers from (B) in sTOs. Color of dots denote average expression, whereas size represents percentage of cells in a cluster expressing the gene of interest.

Cell Type Deconvolution of Trophoblast Populations in sTOs Using Spatial Transcriptomics

To define trophoblast populations within sTOs, we performed cell type deconvolution by integrating the single-cell transcriptomics dataset from sTOs with the spatially resolved transcriptome of the swine maternal-fetal interface. To do this, we filtered the Visium dataset to only include trophoblast populations, specifically clusters 5, 8, and 9 (**Figure 5A-B**). Next, we integrated the single cell RNA-sequencing data from sTO with the Visium spatial transcriptomics dataset. For cell type prediction, we applied a previously established probabilistic modeling algorithm, which leverages the likelihood of gene expression patterns across datasets to assign

315 cluster identities in a spatial context. This analysis enabled us to predict the identities of sTO
316 clusters with high confidence. We found that sTO cluster 0 very strongly mapped to interface
317 trophoblasts, whereas sTO clusters 1, 3, and 4 map to areola-2 and areola-1 trophoblast clusters
318 (**Figure 5D-E, Supplemental Figure 3A, 3B**). In contrast, cluster 2 did not exhibit strong mapping
319 to any structure (**Figure 5D, 5E, Supplemental Figure 3A, 3B**). However, this cluster expressed
320 high levels of the proliferation-associated genes TOP2A and MKI67, suggesting that it
321 represented the stem/progenitor cell population, which is likely present at very low abundance in
322 tissue at the stage of gestation when we were collecting the tissues (**Figure 5F**).

323 We then identified shared markers between sTO clusters and their corresponding spatial
324 transcriptomics clusters to determine the gene expression signatures that defined these
325 mappings. We found that sTO cluster 0 cells expressed 49 markers that were conserved in
326 interface-trophoblasts, which included AKR1B1, HAVCR1, PLA2R1, and TGM2 (**Figure 5F, 5G,**
327 **Supplemental Table 3**). Similarly, sTO cluster 1 expressed 56 shared markers with areola-2
328 cluster, including cathepsins A and D (CTSA and CTSD), NPL and NUPR1 (**Figure 5F, 5G,**
329 **Supplemental Table 4**). sTO cluster 3 had 26 shared markers with areola-2 cluster, with both
330 clusters highly expressing PSAP, FTL, MDK, and B2M (**Figure 5F, 5G, Supplemental Table 5**).
331 Conversely, sTO cluster 4 expressed only 14 shared markers to areola-1 cluster, largely including
332 COX1, COX3, ND4, and CYTB (**Figure 5F, 5G, Supplemental Table 6**). Using this approach,
333 we were able to assign cellular identities and identify shared gene expression profiles for all
334 trophoblast populations within sTOs, which were distributed at similar ratios across independent
335 lines (**Figure 5H**).

336

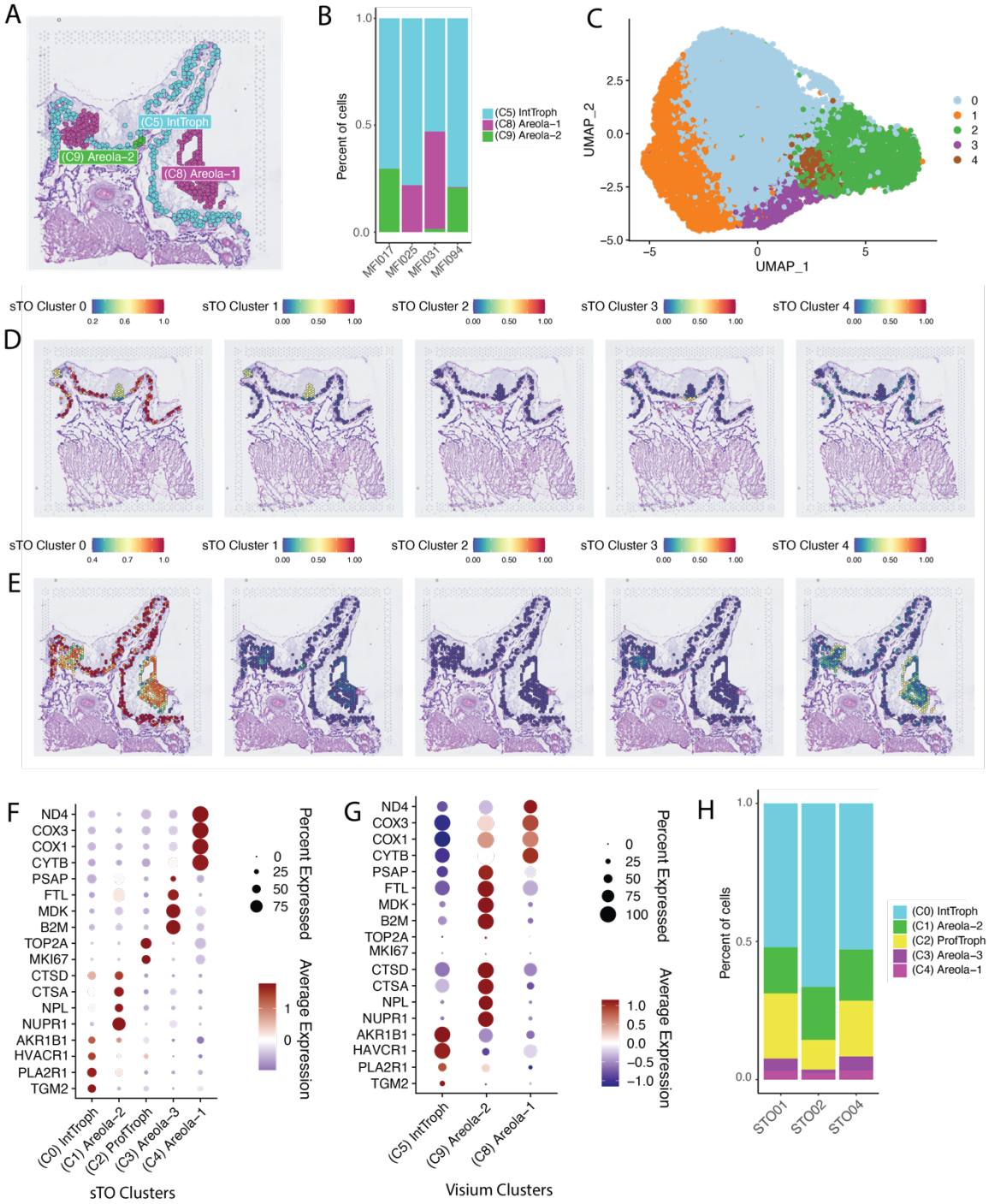

Figure 5: Integration of sTOs and Spatial Transcriptomics Datasets Enables Precise Cellular Identification and Classification. A) Spatial Dim-Plot showing facetted clusters from a representative maternal-fetal interface. As shown Areola-1, Areola-2 and Interface-Trophoblasts were included in this analysis. **B)** Stacked bar-plot showing relative proportions of various clusters across individual maternal-fetal interfaces. **C)** UMAP of sTOs clusters obtained via single cell RNA-sequencing (n = 3 lines). **D-E)** Spatial feature plot showing prediction scores for each spot in the spatial dataset subsetted by sTO cluster. Color shown indicates probability that the

classified sTO cluster is localized to a given position within the spatial dataset. **F-G)** Dot-plot showing the localization of shared markers between the sTO clusters (F) and maternal-fetal interface clusters (G) Color of dots denote average expression, whereas size represents percentage of cells in a cluster expressing the gene of interest. **H)** Stacked BarPlot showing the relative proportion and identity of sTO cell populations.

Pathway Analyses Reveals Conserved Functional Niches of sTO Cell Populations

In vivo, interface trophoblasts and areola trophoblasts have distinct functions. Our data indicated that sTOs differentiated into both of these populations, yet whether these populations retained the functional capacity of their *in vivo* counterparts remained unclear. To this end, we examined the functional pathways active in both sTOs and tissues across trophoblast subpopulations. Given that IntTroph and Areola-2 clusters had the highest probability scores and shared markers between sTO and tissue, we chose to focus this analysis on these two clusters. We performed differential expression analysis between interface trophoblasts and areola-2 trophoblasts, finding that expressional patterns between these two trophoblast populations were starkly different in both the tissue and sTO (**Supplemental Figure 4A, 4B**). Using GO-Term analysis we identified enriched pathways for areola-2 and interface trophoblasts, several of which were enriched in both sTOs and tissue analysis (**Supplemental Figure 4C-F)**. Notably, we found that interface trophoblasts are enriched in GO terms such as extracellular matrix, focal adhesions, and angiogenesis (**Supplemental Figure 4C, 1D**). Conversely, areola-2 clusters were enriched primarily in GO terms surrounding endosome formation (**Supplemental Figure 4E, 4F)**. Expression of various endosome related genes demonstrated that areola-2 clusters in sTOs and tissue Visium datasets were are highly enriched in endosomal markers, whereas interface trophoblasts distinctly lack endosomal gene expression (**Supplemental Figure 4G,H)**. Taken together these data demonstrate that sTOs retain at least some key functions of the corresponding tissue populations, highlighting their utility for studying swine placental biology.

Trajectory Inference Reveals Trophoblast Differentiation Pathways in sTOs

373 Organoids provide a powerful model for defining differentiation trajectories, as they enable the
374 study of cell fate transitions from progenitor cells to more differentiated cell states in a controlled
375 environment. We applied Slingshot trajectory analysis to sTOs to trace the dynamic progression
376 of trophoblast cells along distinct developmental pathways. To do this, we first subsetted the sTOs
377 single-cell dataset to include major cell populations, which included proliferating trophoblasts
378 (ProfTroph), interface trophoblasts (IntTroph), and Areola-2 trophoblasts. We then performed
379 Slingshot trajectory analysis without predefining a starting or ending cluster along the
380 differentiation trajectory. This analysis revealed a single differentiation trajectory, starting in
381 ProfTroph, progressing through IntTroph, and terminating in Areola-2 (**Figure 6A**). To define gene
382 expression changes along this trajectory, we applied the fitGAM function to model dynamic gene
383 expression patterns to assess how specific gene expression profiles evolved across the different
384 stages of trophoblast differentiation. Many genes were temporally regulated along the trajectory,
385 with some showing distinct patterns of upregulation and downregulation, while others exhibited
386 cyclical regulation across the different stages of trophoblast differentiation (**Figure 6B,**
387 **Supplemental Figure 7**). Notably, TOP2A, HMGB2, and PRC1 were strongly downregulated
388 along the trajectory, suggesting a loss of a proliferative capacity as differentiation progresses
389 (**Figure 6B, 6C**). In contrast, GRN and ITM2C, both of which are known to be expressed in the
390 swine placenta, were markedly increased in expression in IntTroph, but then became
391 downregulated in the Areola-2 differentiated state (**Figure 6D, left**). Similarly, several genes
392 including NUS1, NUPRR1, SQSTM1, and ARF4 all increased in expression at the terminal areola-
393 2 differentiation stage (**Figure 6E, 6F**, left). To validate these findings from the trajectory analysis
394 of sTOs, we compared the gene expression patterns to the Visium spatial transcriptomics data.
395 This comparison revealed a high level of concordance between the temporally regulated markers
396 identified in sTOs and their expression in corresponding tissue structures, further confirming that
397 sTOs effectively recapitulate the differentiation processes observed *in vivo* (**Figure 6D-F,**
398 **Supplemental Figure 5A-F**).

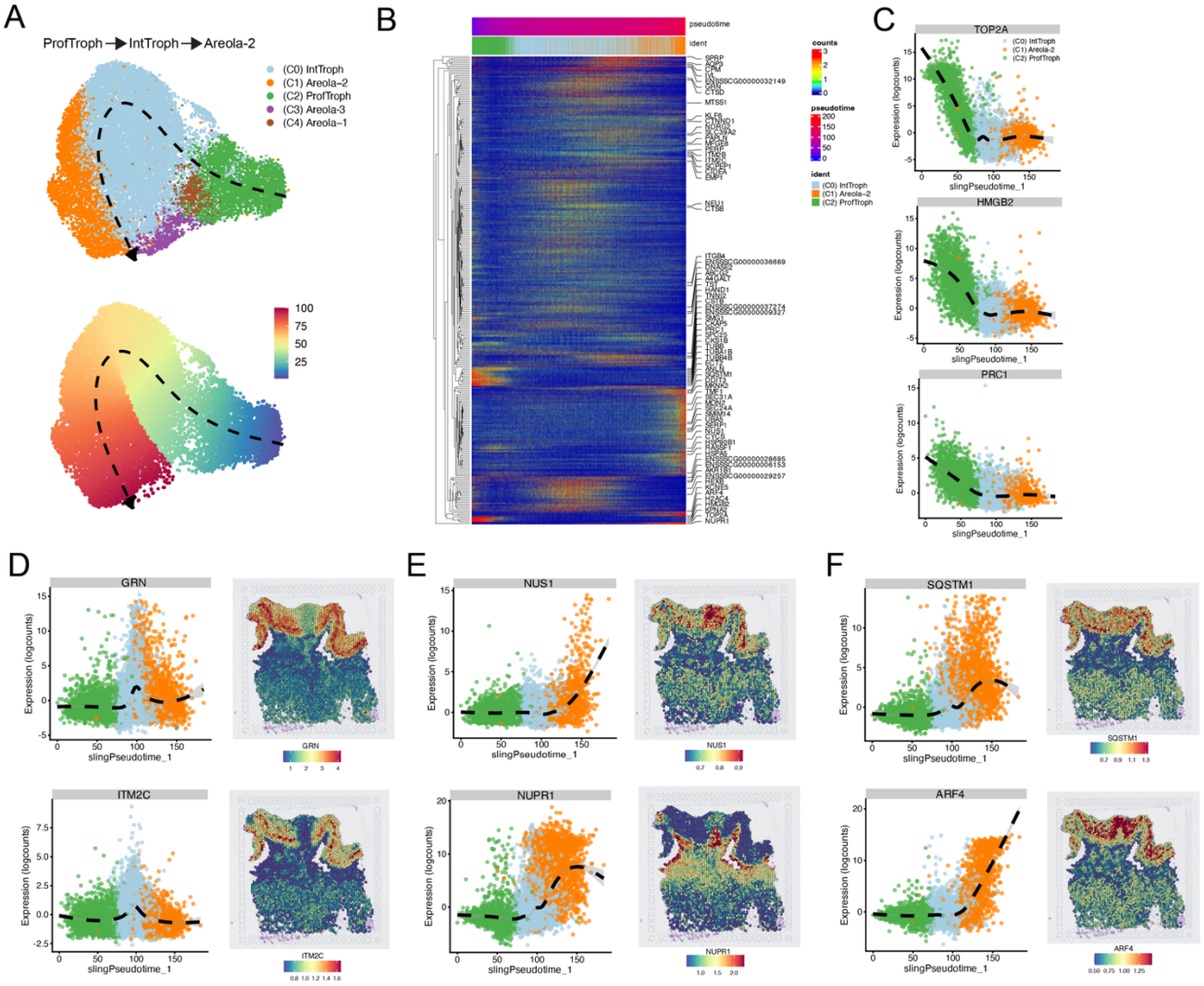

Figure 6: Trajectory Analysis Reveals the Differentiation Pathway of Swine Trophoblasts. A) UMAPs showing Slingshot calculated trajectory of trophoblasts within sTO. Top panel shows the trajectory across labeled clusters, whereas bottom panel shows the trajectory across a pseudotime. **B)** Heatmap showing temporally regulated genes across the calculated pseudotime trajectory. Individual columns represent individual cells that are ordered along the calculated pseudotime. Identities are positions along the pseudotime are shown above the heatmap. **C)** Representative expression plots showing gene expression changes along the calculated pseudotime that are enriched in the proliferative stem cell population. **D)** Representative expression plots and spatial feature plots showing genes that are enriched during the transition to Interface-Trophoblasts and their expression pattern within our spatial transcriptomics dataset. **E-F)** Representative expression plots and spatial feature plots showing genes that are enriched during the transition to Areola-2 trophoblasts and their expression pattern within our spatial transcriptomics dataset.

414 **Cell-Cell Interaction Networks at the Swine Maternal-Fetal Interface Through Comparative**
415 **Analysis of sTOs and Spatial Transcriptomics**

416 Maternal-fetal crosstalk has been widely studied in human pregnancy, where it plays crucial roles
417 in nutrient exchange, immunological tolerance, and successful placentation[36-38]. Recent evidence
418 suggests that similar communication processes take place in the peri-implantation porcine
419 embryo and the maternal endometrium, highlighting the importance of defining these interactions
420 in the swine placenta[39,40]. To delineate communication networks at the swine maternal-fetal
421 interface, we used CellChat to define cell-cell signaling pathways and assess how well these
422 interactions are recapitulated in sTOs. CellChat is based on a comprehensive dataset of known
423 ligand-receptor pairs, using their expression to infer communication between cells. In spatially
424 resolved data, CellChat also incorporates the physical distance between tissue sites, filtering out
425 interactions that are unlikely to occur due to the spatial separation between these sites. This
426 analysis revealed extensive crosstalk in sTOs (**Figure 7A**) and in maternal-fetal interface tissue
427 (**Figure 7B**). In sTOs, the strongest communication was observed from Areola-1, Areola-3, and
428 interface trophoblasts (IntTroph), which exhibited interactions with all other populations (**Figure**
429 **7C**). In tissue, the myometrium (Myo, which was merged into a single cluster for this analysis)
430 and the vasculature (Vasc) were responsible for the most robust communication, while the
431 interstitium (Ist), endometrium (Endo), Areola (merged into a single cluster), and IntTroph showed
432 the weakest number of communication networks (**Figure 7D**). Notably, all maternal clusters were
433 able to crosstalk with the fetal trophoblast populations except the myometrium and vasculature
434 (**Figure 7B, 7D**).

435 Using CellChat, we classified both outgoing and incoming signaling patterns in tissue and
436 sTOs. This analysis revealed similarities and differences in communication networks between the
437 two datasets, offering insights into conserved signaling pathways and cell-cell interactions. We
438 identified three distinct communication patterns within sTOs: pattern 1, associated with Areola-1,
439 IntTroph, and proliferating trophoblasts (ProfTroph); pattern 2, exclusive to Areola-3; and pattern

440 3, specific to Areola-2 (**Figure 7E**). Each pattern corresponded to distinct communication
441 networks, with LEP and NEGR in pattern 1, NCAM and IGF in pattern 2, and NECTIN, ESAM,
442 and EGF in pattern 3 (**Supplemental Figure 6C, 6D**). In the spatial dataset, pattern 1
443 communication was shared between the uterine epithelium (UtEp), blood, and endometrium
444 (Endo); pattern 2 was restricted to Myo; and pattern 3 was shared among fetal-derived
445 populations, including the Ist, IntTroph, and Areola (**Figure 7F, Supplemental Figure 6A, 6B**).
446 Next, we analyzed CellChat datasets to identify shared and distinct communication
447 networks between trophoblasts in sTOs and spatial tissue. Notably, several pathways enriched in
448 the fetal compartment of the spatial dataset were also enriched in sTOs, particularly the Granulin
449 (GRN) and Midkine (MK) pathways (**Figure 7G-7N**). In tissue, both areola and interface
450 trophoblasts acted as senders and receivers for MK and GRN pathways (**Figure 7G, 7K**). While
451 GRN signaling between interface and areola trophoblasts was not detected in tissue, autocrine
452 signaling within areola trophoblasts was observed (**Figure 7G**). Spatial transcriptomics confirmed
453 the expression patterns of these ligand-receptor pairs, consistent with CellChat predictions
454 (**Figure 7H, 7L**). In sTOs, a similar pattern emerged, with areola and interface trophoblasts acting
455 as senders and receivers for GRN and MK pathways (**Figure 7I, 7M**). The cellular heterogeneity
456 of sTOs allowed us to detect differences in signaling capacity among areolar trophoblast
457 populations, with Areola-3 being the dominant sender of MK signaling due to higher MDK
458 expression (**Figure 7M**, **7N**). sTOs also effectively recapitulated GRN signaling pathways,
459 consistent with the tissue data (**Figure 7I, 7J**). In sTO, Areola-1, interface trophoblasts, and
460 proliferative trophoblasts were the primary senders of GRN, largely due to their higher GRN
461 expression, with Areola-2 as the main receiver (**Figure 7J, 7N**). Furthermore, as observed in the
462 tissue, areolar trophoblasts did not send GRN signals to interface trophoblasts in sTOs (**Figure**
463 **7I**). Taken together, these findings indicate that sTOs replicate key signaling networks present in
464 the porcine placenta.
465

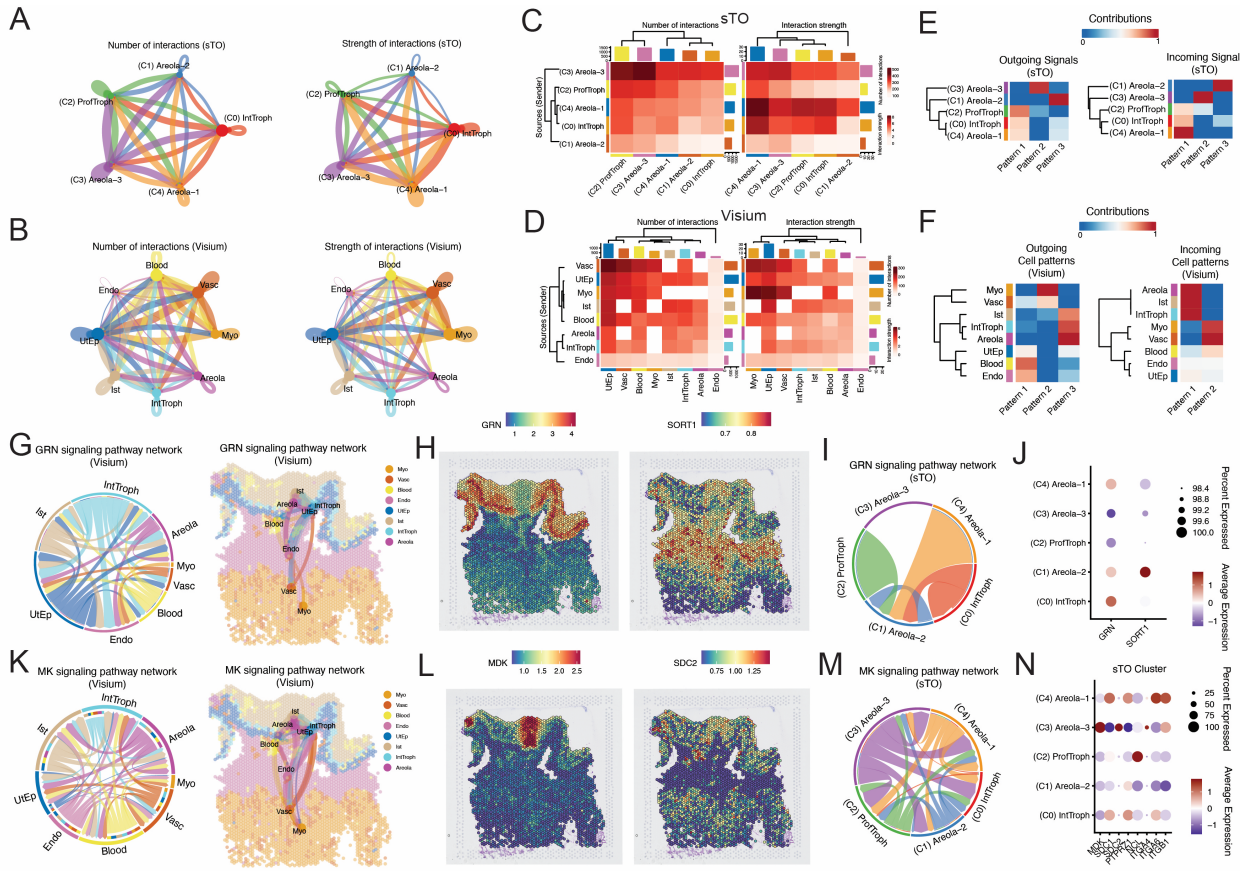

Figure 7: sTOs Recapitulate Crosstalk Pathways Within the Swine Placenta. A) Chord diagrams showing the number (Left panel) and strength (right panel) of calculated inter-cluster interactions within sTO. **B)** Chord diagrams showing the number (Left panel) and strength (right panel) of calculated inter-cluster interactions within the porcine maternal-fetal interface. **C)** Heatmap showing the number (left panel) and strength (right panel) of interactions between clusters within sTO. Color indicates increased number (left) or strength (right) between the sending cluster and the receiving cluster. **D)** Heatmap showing the number (left panel) and strength (right panel) of interactions between clusters within the porcine maternal-fetal interface. Color indicates increased number (left) or strength (right) between the sending cluster and the receiving cluster. **E)** Heatmap showing patterns signaling patterns within sTO. Left panel shows outgoing signaling patterns whereas the right panel shows incoming signaling patterns. Color indicates how strongly a given cluster aligns with a specific pattern. **F)** Heatmap showing patterns signaling patterns within the porcine maternal-fetal interface. Left panel shows outgoing signaling patterns whereas the right panel shows incoming signaling patterns. Color indicates how strongly a given cluster aligns with a specific pattern. **G-J)** Plots showing GRN signaling within both sTO and the maternal-fetal interface. G) Diagrams showing GRN signaling within the maternal-fetal interface. Left panel shows a chord diagram, whereas the right panel shows the spatial localization of these interactions. H) Spatial feature plot showing the localization of GRN pathway specific genes. I) Chord diagram showing GRN signaling within sTO. J) Dotplot showing the cluster specific expression of GRN pathway gene expression in sTO. Color of dots denote average expression, whereas size represents percentage of cells in a cluster expressing the gene of interest. **K-N)** Plots showing MK signaling within both sTOs and the maternal-fetal interface. K) Diagrams showing MK signaling within the maternal-fetal interface. Left panel shows a chord diagram, whereas the right panel shows the spatial localization of these interactions. L) Spatial

feature plot showing the localization of MK pathway specific genes. **M)** Chord diagram showing MK signaling within sTO. **N)** DotPlot showing the cluster specific expression of MK pathway gene expression in sTO. Color of dots denote average expression, whereas size represents percentage of cells in a cluster expressing the gene of interest.

DISCUSSION

US agricultural commodities from swine account for approximately $62 billion in added economic value and is heavily reliant on successful animal husbandry[41]. In all eutherian mammals, including swine, successful placentation is critical for fetal growth and survival[7]. Therefore, understanding non-human placental function, development, and defenses is critical for ensuring continued reproductive success. While there is growing interest in studying non-human placentation, the lack of appropriate models remains a major hurdle. We and others have demonstrated that trophoblast organoids derived from human placentae are a critical tool for the study of human placentation due to their ability to be passaged, cryopreserved, and to recapitulate human trophoblast heterogeneity[28,30,42]. Here, we report the establishment of sTOs, which recapitulate key aspects of the swine placenta.

We show that sTOs can be derived from full-term swine placentae, enabling model establishment without the need to sacrifice animals. Like hTOs, sTO can be expanded, cryopreserved, and successfully recovered, making them an ideal *in vitro* model. Current models, such as PTr2 cells, contain a unique expressional profile to swine placental tissue, and express low levels of several trophoblast markers. We show here that sTOs express high levels of the trophoblast markers KRT18, ELF3, and GATA3, and an expressional signature more consistent with swine placentae. Importantly, sTOs cultured within Matrigel spontaneously form an interiorly localized apical surface that is reversible by culturing in suspension, thereby allowing for customization of this model. Together, our data suggest that sTOs better recapitulate the transcriptional signature of swine placental tissue than currently available *in vitro* models.

As discussed previously, the swine placenta is distinct from the human placenta at both a structural and cellular level[7]. In humans, placental trophoblasts fall into several distinct

519 subpopulations including CTBs, EVTs, and the STB, all of which have distinct roles in the
520 formation of the hemochorial placenta[7]. In the epitheliochorial placenta, such as those found in
521 swine, there is no direct contact between maternal blood and fetal trophoblasts, which
522 theoretically could limit the efficiency and molecular breadth of nutrient transfer to the developing
523 fetus[7,8]. To facilitate this exchange, the highly folded interface expresses various nutrient
524 transporters and aquaporins[18,19]. Further, the porcine placenta contains a specialized structure
525 known as an areola, which is a dome like cluster of trophoblasts that sit atop uterine glands[20].
526 These structures, which have a peak density of approximately 2500 per placenta[43], collect and
527 transfer maternally-derived histotroph to the fetus as a nutrient source. Indeed, previous studies
528 have indicated that areola surface area is directly correlated with fetal growth, further supporting
529 their critical role in nutrient acquisition[43]. Interestingly, areola structures have been noted in many
530 ungulates, including hippopotamuses[44], dolphins[45], and llamas[46], suggesting that areola are
531 critical for fetal growth across species. Several studies have indicated that these porcine
532 trophoblast subpopulations have some degree of cellular heterogeneity *in vivo.* It is known that
533 along placental folds of the interface, expression of various transporters varies. For example,
534 GLUT1 and GLUT8 have opposing expression profiles, with GLUT1 being located at the base of
535 the folds and GLUT8 being localized to the tip of the folds[35]. Similar spatially localized gene
536 expression has been observed for aquaporins[18]. Additionally, trophoblasts localized to the areola
537 have increased expression of CTSL, AQP5, and ITGB3 relative to other trophoblast
538 populations[18,22,47]. How these various populations differentiate and develop is largely unknown,
539 primarily due to the lack of an *in vitro* model that provides this cellular heterogeneity without the
540 need to consistently access fresh tissue.

541 We and others have previously demonstrated that in human trophoblast organoids, there
542 is extensive cellular heterogeneity, indicating that trophoblast organoids spontaneously
543 differentiate into the various trophoblast populations of the placenta[28-30,48]. Single cell RNA-
544 sequencing of sTO revealed similar cellular heterogeneity within this organoid model. While

545 previous studies have identified markers of various trophoblast subpopulations in swine
546 placentae[18,22,35], these markers were insufficient to segregate sTO cell populations. Using Visium
547 spatial transcriptomics of mid-gestation swine maternal-fetal interfaces, we defined the
548 transcriptomic landscape of swine trophoblast populations *in situ*. By coupling a single cell
549 RNASeq dataset from sTOs and Visium spatial transcriptomics dataset from swine placentae, we
550 were able to assign identities to sTOs populations using an unbiased probabilistic modeling
551 approach. Simultaneously, we identified a shared gene expression profile between sTO cell
552 populations and their corresponding placental cell populations. Using this approach, we
553 demonstrate that sTOs contain a proliferative stem cell population, an interface trophoblast
554 population and three areola trophoblast populations. Critically, this approach allowed for robust
555 identification of cell populations in an unbiased manner.

556 Using trajectory analysis, we defined how sTOs gain their heterogeneity. Using Slingshot,
557 we demonstrate that proliferative stem cells differentiate into interface trophoblasts, which can
558 then differentiate into areola-2 trophoblasts. This analysis uncovered numerous expression
559 changes throughout the differentiation process, including novel targets like ITM2C and NUPR1,
560 which could be investigated in future mechanistic studies to enhance our understanding of swine
561 placental development. Having defined the expressional changes along this trajectory, we then
562 confirmed their localization in tissue finding high concordance between sTOs and tissue level
563 expression, suggesting a shared trajectory between these two systems. By comparing global
564 gene expression changes in sTO derived interface trophoblasts and areola-2 trophoblasts we go
565 on to show that these two populations display starkly different functional niches, with interface
566 trophoblasts being primed to form focal adhesions and promote angiogenesis, whereas areola-2
567 trophoblasts were enriched in programs for the formation of endosomes. It is noted within the
568 literature that areola trophoblasts contain a high number of intracellular vesicles, presumably to
569 facilitate transport of histotroph across this epithelial barrier[20]. As expected, when we examined
570 the expression of key endosome markers within the tissue and sTO, we observed similar patterns

571 of expression, with endosome markers expressed at a higher level in areola-2 cells compared to
572 interface trophoblasts. Together, these data demonstrate that sTOs recapitulate the
573 developmental and functional differences in trophoblast populations observed in the porcine
574 placenta, highlighting their utility in studying porcine placental development.

575 While integrating sTO and spatial datasets allowed for robust cell cluster identification,
576 parallel analyses enabled us to further explore the functional similarities between sTOs and
577 placental tissue. Applying CellChat to these datasets revealed that several key signaling
578 pathways are conserved between sTOs and placental tissue. For example, the Midkine (MK) and
579 Granulin (GRN) pathways, represented pathways that showed a high degree of intra-placental
580 communication in placental tissue. These pathways, which have been shown to be active in the
581 placenta and critical for fetal and placental development, were similarly highly active within sTO[49-
582 53]. Importantly, sTO recapitulated autocrine and paracrine signaling patterns observed in placental
583 tissue, highlighting their utility as a physiologic model. Although we did detect crosstalk between
584 proliferative stem cells and other trophoblasts within sTO, these events were not observed within
585 the Visium dataset due to the low occurrence of stem cells within the tissue. Due to their high
586 abundance within sTO we were able to capture crosstalk events in this rare population,
587 highlighting the utility of sTO in defining novel crosstalk events in rare cell populations.

588 Previous studies have used single cell RNA-sequencing to characterize the porcine uterus
589 and embryos[39,40,54]. However, these studies rely on existing markers to assign cellular identity,
590 lack histological structural context, do not provide spatial segregation of gene expression
591 signatures, and were not performed at a gestational stage where critical structures, such as the
592 areola, are present. Our data robustly define the expression profiles of various histological
593 structures at the swine maternal-fetal interface. By mapping gene expressions directly to
594 corresponding histological structures, we confirmed cellular identities without relying on
595 conventional markers, making this assignment unbiased. Moreover, using mid-gestation swine
596 maternal-fetal interfaces, we were able to characterize the expression profiles of key structures,

597 including the areola and the interface, which have previously eluded detailed analyses. This
598 dataset provides new insights into placental biology that were not achievable with earlier
599 approaches.

600 Demonstrating the utility of this spatially resolved dataset, we identified two
601 transcriptionally and structurally distinct areola populations within the porcine placenta: Areola-2,
602 which appears continuous with the interface trophoblasts, and Areola-1, which is localized
603 primarily to the placental interstitium without evidence of direct contact with the interface. This
604 finding emphasizes the power of spatial transcriptomics in revealing previously unrecognized
605 cellular diversity within within structurally complex tissues such as the placenta. While both
606 clusters expressed high levels of the known areola marker CTSL[22], these clusters had divergent
607 gene expression profiles with Areola-2 expressing high levels of MDK, CTSD, PAG2L2 and
608 Areola-1 expressing high levels of CCDC162, SPINK4, and MMP25. While it remains unclear why
609 these two areola populations exist, previous results[22] have shown that histologically similar CTSL
610 positive structures exist within the porcine placenta. It is possible that these represent areola at
611 different stages of development, with Areola-1 representing a more mature population due to its
612 higher expression of CTSL and its increased size. Together, these findings highlight the power
613 and utility of the spatial transcriptomic dataset in advancing our understanding of the fundamental
614 biology of the porcine placenta.

615 Our work offers a comprehensive characterization of spatial gene expression in the
616 porcine placenta and successfully establishes an organoid model that captures its cellular
617 heterogeneity. However, limitations include the resolution of Visium spatial transcriptomics, which
618 does not allow for single-cell level definition of histological populations. For example, the identified
619 Visium clusters may represent a mixture of gene expression profiles but nonetheless captures
620 the dominant signals of key structures and cell populations. For instance, although we observed
621 some overlap in marker expression between uterine epithelium and trophoblast populations,
622 these clusters still separate along the interface. Moreover, the populations are strongly

represented by known markers, indicating that despite resolution constraints, this technique effectively segregates distinct populations and provides robust biological insights. Another limitation of this study is that we focused on a single mid-gestation timepoint. While this provides valuable insights into the biology of the porcine placenta during this stage, it limits our ability to assess dynamic changes in cellular composition and signaling across different stages of gestation. While previous studies have highlighted that human trophoblast organoids represent first trimester tissue[29,31], our bulk RNA-seq data demonstrated that sTOs have similar expression to porcine placentae regardless of gestation. It remains possible that early or later gestation placentae would have mapped with higher probabilities to sTO populations enabling more robust identification. Future studies aimed at capturing multiple gestational timepoints in the porcine placenta are therefore warranted. While the data presented here demonstrate the utility and strength of spatial transcriptomics, they represent only a portion of the insights generated in this study. The thousands of spatially resolved genes and pathways identified provide a valuable resource for advancing porcine reproductive biology. To facilitate broader access, we have developed a user-friendly web-based app, enabling researchers without advanced computational resources to explore and analyze the data (see data availability statement for further details)

Taken together, our study describes the derivation of an organoid model that recapitulates the cellular heterogeneity and functionality of the swine placenta. Additionally, we provide a spatially resolved expression landscape of the swine maternal-fetal interface, creating a valuable resource for the study of non-human placentation. The ability to map gene expression directly to histological structures offers unprecedented insights into the cellular dynamics of the porcine placenta, setting a new benchmark for comparative placental biology research. These findings have the potential to significantly advance our understanding of placental biology across eutherians, offering a critical framework for studying key aspects of maternal-fetal communication and placental development. Moreover, the organoid model and spatial transcriptomic data will

648 serve as foundational tools for exploring mechanisms of placental function and dysfunction, with
649 broader implications for reproductive biology and veterinary medicine.
650
651 **METHODS**
652 **Animal Husbandry and Tissue Collection**
653 *Tissue Collection for sTO Derivation*
654 Placentae for swine trophoblast organoids (sTO) were collected from crossbred sows consisting
655 of Yorkshire, Large White, and Landrace breeds from the North Carolina State University (NCSU)
656 Swine Educational Unit (SEU), which is a facility free from Porcine Reproductive and Respiratory
657 syndrome virus (PRRSV), swine influenza A virus and mycoplasma species. The average
658 gestation length of sows at the SEU is 114.2 +/- 1.3 days. At SEU older parity sows (n = 2; parity
659 5) that didn't farrow by 114 days were induced using 2mL of Lutalyse (Dinoprost tromethamine
660 injection, Zoetis) intramuscularly, whereas gilts (n=1) were allowed to farrow naturally. Placentae
661 collected from gilts or sows were placedin ziploc bags containing Dulbecco's Modified Eagle
662 Medium (DMEM, Cytiva Hyclone cat. # SH30081.01) supplemented with 10% inactivated fetal
663 bovine serum (FBS, Biowest #S1620 Heat Inactivated, USDA approved origin), 1100 IU/mL
664 penicillin, 1100 mg/mL streptomycin (Cytiva Hyclone 100x solution, #SV30010), 2 mM L-
665 glutamine (GIBCO 100x 200mM, #A2916801), Amphotericin B 2.5 µg/ml (Gibco, Fungizone,
666 15290-018)). Placentae were collected under experimental procedures approved by the NCSU
667 Institutional Animal Care and Use Committee (IACUC) ID# 22-122-B (n=2, gilts, IM Lutalyse
668 injection) or via normal farrowing activities performed in NCSU SEU (n=3))
669
670 *Tissue Collection for Visium Spatial Transcriptomics*
671 Animal procedures carried out in compliance with Purdue University's animal care policies and
672 approved by the Institutional Animal Care and Use Committee (IACUC Protocol #2104002130),
673 and as previously described [55]. In short, a total of n=3 commercial landrace/large white composite

674 gilts, were selected from the Animal Sciences Research and Education Center (ASREC) at
675 Purdue University, synchronized with oral progestogen (Altrenogest at 17.6 mg/day for 14 days).
676 Following withdrawal, the gilts were heat checked twice daily with an intact boar, and artificially
677 inseminated 12 hours after the first observed lordosis responses, and every 24 hrs there after
678 until the end of estrus. Pregnancy was confirmed via transcutaneous ultrasound on gestation day
679 30-35. Gilts were fed a standard gestation diet comprised of corn, soybean meal and dried
680 distillers grain, and formulated to meet the dietary requirements as outlined by the NCR. On
681 gestation day 65 (relative to first artificial insemination) pregnant gilts were stunned with a
682 penetrating captive bolt and euthanized via rapid exsanguination. The gravid uterus carefully
683 extracted though a midline incision and linearized such that each fetus and its corresponding
684 placenta could be isolated. Sections of the maternal fetal interface were collected adjacent to the
685 umbilical stump and a roughly 1 cm^2 section of intact placenta (maternal and fetal tissue) was
686 excised, embedded in optimal cutting temperature media (OCT) (Tissue-Plus OCT Compound;
687 Fisher Scientific)and slowly cooled to cryogenic temperature using dry ice.
688

689 **Derivation, culture, and passaging of sTO**

690 sTOs were derived using a previously established method used for the derivation of human
691 trophoblast organoids[29]. Briefly, placentae were extensively rinsed with Phosphate Buffered
692 Saline (PBS) and sequentially digested with 0.2% trypsin-250 (Alfa Aesar, J63993-09)/0.02%
693 EDTA (Sigma-Aldrich, E9884-100G) and 1.0 mg/mL collagenase V (Sigma-Aldrich, C9263-
694 100MG). Digested tissue was then disrupted by pipetting up and down vigorously ~10 times with
695 10 mL serological pipette (VWR, 89130-898; MSP, 62-1005-10) and pooled prior to washing with
696 Advanced DMEM/F12 medium (Life Technologies 12634-010). Pelleted digests were then
697 resuspended in ice-cold growth-factor reduced Matrigel (Corning 356231). Matrigel 'domes'
698 (40 µL/well) were plated into 24-well tissue culture plates (Corning 3526), placed in a 37° C
699 incubator to pre-polymerize for ~3 min, turned upside down to ensure equal distribution of the

700 isolated cells in domes for another 10 min, then overlaid with 500 µL prewarmed term trophoblast
701 organoid medium (tTOM).
702
703 tTOM consisted of Advanced DMEM/ F12 (Life Technologies, 12634-010) supplemented with 1×
704 B27 (Life Technologies, 17504-044), 1× N2 (Life Technologies, 17502-048), 10% fetal bovine
705 serum (FBS) (vol/vol, Cytiva HyClone, SH30070.03), 2 mM GlutaMAX supplement (Life
706 Technologies, 35050-061), 100 µg/mL Primocin (InvivoGen, antpm-1), 1.25 mM N-Acetyl-L-
707 cysteine (Sigma-Aldrich, A9165), 500 nM A83-01 (Tocris, 2939), 1.5 µM CHIR99021 (Tocris,
708 4423), 50 ng/mL recombinant human EGF (Gibco, PHG0314), 80 ng/mL recombinant human R-
709 spondin 1 (R&D systems, 4645-RS-100), 100 ng/mL recombinant human FGF2 (Peprotech, 100-
710 18C), 50 ng/mL recombinant human HGF (Peprotech, 100-39), 10 mM nicotinamide (Sigma-
711 Aldrich, N0636-100G), 5 µM Y-27632 (Sigma-Aldrich, Y0503-1MG), and 2.5 µM prostaglandin E2
712 (PGE2, R&D systems, 22-961-0).
713 Cultures were maintained at 37° C in a humidified incubator with 5% CO2. Medium was
714 renewed every 2–3 days. Small trophoblast organoid spheroids became visible by approximately
715 7-10 days post isolation. Derived sTO were passaged every 5–7 days depending on their size
716 and density. To passage, spent media was removed from sTO and fresh Advanced DMEM/F12
717 added to the well. Domes were disrupted using a pipet tip and pelleted via centrifugation. Pellets
718 were then digested in prewarmed TrypLE Express (Life Technologies, 12605- 028) at 37° C for
719 5–7 min. Pelleted organoids were then further dissociated manually using a P200 pipette by
720 vigorously pipetting approximately 200-300 times. Dissociated sTOs were pelleted and
721 resuspended in fresh ice-cold Matrigel and replated as domes at the desired density for
722 continuous culture. All experiments described in this paper were performed in sTOs under
723 passage 15 to limit potential passage level effects.

724 For cryopreservation, sTOs were grown to high density and spent media was aspirated.
725 CryoStor CS10 (Stem Cell Technologies; # 07930) was then added 1mL per 'dome' and domes
726 disrupted using a p1000 pipette. Organoids were then transferred to a sterile cryovial and
727 gradually frozen to -80°C using a CoolCell (Corning). After 24 hours vials were transferred to
728 vapor phase liquid nitrogen for long term storage. To thaw cryopreserved organoids, cryovials
729 were rapidly thawed (<2min) in a 37°C water bath with gentle agitation. Freezing media and
730 organoids were then transferred to a 15mL conical and resuspended 9mL of prewarmed
731 Advanced DMEM/F12. Organoids were then pelleted and resuspended in ice cold Matrigel and
732 seeded into 'domes' in 24 well plates. Fresh tTOM including 5 μM Y-27632 (Sigma-Aldrich,
733 Y0503-1MG) was added prior to incubation for 24-72 hours at 37°C with 5% CO_2. sTO were then
734 passaged as described above.
735

736 **Reversal of sTO Polarity**

737 To reverse organoid polarity, we utilized a previously established protocol we developed to invert
738 hTOs[28]. Briefly, spent media was removed and 1mL of ice-cold cell recovery media (Corning Cat#)
739 added to each well. Domes were gently disrupted using a P1000 and organoids transferred to a
740 15mL conical. Organoids were incubated for 30 minutes on ice to dissolve Matrigel prior to being
741 washed twice using 1x DPBS. Organoids were then resuspended in 500mL of prewarmed TOM
742 and plated into ultra-low binding 24 well plates. Organoids were incubated statically at 37°C with
743 5% CO_2 for 48 hours prior to usage.
744

745 **Histology and Immunofluorescence Staining of sTOs**

746 Mature organoids were fixed using 4% paraformaldehyde in PBS for 15 minutes and subsequently
747 washed with PBS. Histology was performed by HistoWiz Inc. (histowiz.com) using a Standard
748 Operating Procedure and fully automated workflow. Samples were processed, sectioned at 5μm.

749 Whole slide scanning (40x) was performed on an Aperio AT2 (Leica Biosystems). For
750 immunofluorescence staining, whole mount staining of organoids was performed using previously
751 described methods with some modifications. Briefly, organoids were removed from PBS and
752 permeabilized for 10 minutes in a permeabilization buffer consisting of 0.5% Triton X-100 and 1%
753 Bovine Serum Albumin (BSA) in PBS. Organoids were then pelleted and stained overnight using
754 a ZO-1 antibody conjugated to AlexaFluor 488 (Santa Cruz) at a dilution of 1:50 in
755 permeabilization buffer. The organoids were then pelleted and washed twice in PBS, prior to
756 staining with Phalloidin conjugated to AlexaFluor 633 (Thermo) according to manufacturer's
757 instructions. Organoids were then pelleted and washed twice in PBS prior to mounting with
758 Vectashield containing DAPI. Slides were then imaged using Olympus Fluoview FV3000 inverted
759 confocal microscope and images processed using FIJI. Brightfield images of whole organoids
760 were obtained from fresh, mature, unfixed wells using a Keyence BZ-X810 all-in-one fluorescence
761 microscope
762
763 **Bulk RNA-Sequencing of sTO**
764 *RNA Isolation, Library Prep, and Sequencing*
765 Total RNA was isolated with the Sigma GenElute total mammalian RNA miniprep kit (Cat #
766 RTN350-1KT) or Qiagen RNAeasy Mini Kit (Cat #74104) following the manufacturer's instruction
767 and using supplementary Sigma DNase digestion. RNA quality and concentration were
768 determined using a Nanodrop ND-1000 Spectrophotometer. For bulk RNA-seq analysis, RNA
769 was isolated from organoids as described above. Purified Total RNA was verified by Thermo
770 scientific Nanodrop one. The libraries were prepared by the Duke Center for Genomic and
771 Computational Biology (GCB) using the Tru-Seq stranded total RNA prep kit (Illumina).
772 Sequencing was performed on the NovaSeq 500 by using 75-bp paired-end sequencing.
773

774 For PTr2 cells, raw reads from a previously published study were downloaded from the Sequence
775 Read Archive (SRA): SRR16912824, SRR16912825, and SRR16912827. Similarly, raw reads for
776 GD60, GD90, and L0 tissues were downloaded from SRA: SRR6703668, SRR6703669,
777 SRR6703670, SRR6703671, SRR6703672, SRR6703673, SRR6703674, SRR6703675,
778 SRR6703676, and SRR6703677.
779
780 *Bulk RNA-seq Analysis*
781 Raw reads were aligned to the swine genome (susScr11) using QIAGEN CLC Genomics (v20).
782 Reads per kilobase per million mapped reads (RPKMs) were compiled from all samples and
783 imported into R for analysis. The packages tidyverse, magrittr, pheatmap, rio, factoextra, ggforce,
784 tidyheatmap, and DESeq2 were utilized for analysis. Principal component analysis was performed
785 using RPKMs with confidence ellipses indicating a 95% confidence interval. Heatmaps were
786 made using pheatmap and tidyheatmap, with row scaling and hierarchical clustering of both rows
787 and columns. For sex determination analyses an established protocol for sexing pigs using bulk
788 rna-sequencing data was utilized, with minor modifications [34]. Briefly, the summation of the
789 following 9 Y-linked genes: EIF2S3Y, ZFY, KDM5D, EIF1AY, DDX3Y, LOC100625207,
790 LOC110257894, LOC110255257, and LOC110255320. Summation scores below 2 are
791 considered female, whereas scores above 2 are considered male.
792
793 **Single-Cell RNA-Sequencing of sTOs**
794 sTO from three independent lines (STO01, STO02, and STO04) were grown to high density using
795 the method above. Spent media was removed from the wells and fresh Advanced DMEM/F12
796 added to the well. Domes were disrupted using a pipet tip and pelleted via centrifugation. Pellets
797 were then digested in prewarmed TrypLE Express (Life Technologies, 12605- 028) at 37° C for
798 10-15 min. Pelleted, digested organoids were then further dissociated using a 23G needle
799 aspirating and ejecting 3 times. For STO01 and STO04 a dead cell removal step was performed

800 (Miltenyi Biotech catalog #: 130-090-101) per manufacturer's instructions. Disassociated sTO
801 were then filtered through a 40um cell strainer, which was subsequently washed using 4mL of
802 Advanced DMEM/F12. Pelleted cells were then resuspended in fresh Advanced DMEM/F12 and
803 placed on ice until viability counts were performed.
804
805 Libraries were prepared following standard 10x Genomics Single Cell Gene Expression 3'
806 protocols. Samples containing highly viable cells (80% viability or higher), were washed and
807 filtered through 40µm filter and resuspended in a 1x PBS / 0.04% BSA buffer, at a concentration
808 of 1000 cells/µL. A Cellometer K2 instrument (Nexcelom - Lawrence, MA) was then used to
809 determine the concentration of the single cell suspension. Cells were then suspended in master
810 mix containing reverse transcription (RT) reagents using a volume equivalent to the target capture
811 number of 10,000 cells (plus approximately 60% overage to account for capture efficiency of the
812 assay). This master mix was loaded onto the 10x microfluidics chip, together with gel beads
813 carrying the Illumina TruSeq Read 1 sequencing primer, a 16bp 10x barcode, a 12bp unique
814 molecular identifier (UMI) and a poly-dT primer, and oil for the emulsion reaction. The Chromium
815 X instrument was then used to generate gel beads in emulsion (GEMS) for the RT and barcoding
816 of single cells. After the RT reaction, the GEMs were broken, full length cDNAs were cleaned with
817 Silane Dynabeads, and then amplified via PCR. Following purification using SPRI bead size
818 selection the cDNAs were assayed on a 4200 TapeStation 4200 High Sensitivity D5000
819 ScreenTape (Agilent - Santa Clara, CA) for qualitative and quantitative analysis.
820
821 Enzymatic fragmentation and size selection were used to optimize the cDNA amplicon size for
822 the sequencing library preparation in which Illumina P5 and P7 sequences (San Diego, CA), a
823 sample index, and TruSeq read 2 primer sequence are added via end repair, A-tailing, adaptor
824 ligation, and PCR. The final libraries contained P5 and P7 primers used in Illumina bridge
825 amplification. Following additional purification libraries were assayed for quality, using a

826 TapeStation HSD1000 ScreenTape, then quantitated and checked for successful adapter ligation
827 with the KAPA Library Quantification Kit (Roche-Indianapolis, IN). Sequences were generated
828 using paired end sequencing on an NovaSeq X Plus, at ~62k reads/cell.
829
830 **Analysis of Single Cell Data**
831 *QC and Cluster Analysis*
832 FASTQ files were uploaded to the 10X Cloud Analysis website
833 (https://www.10xgenomics.com/products/cloud-analysis) and analyzed using cellranger v7.1.0
834 using Sus scrofa genome v11.1 downloaded from Ensembl (www.ensembl.org). Mapped files
835 were downloaded through command line and filtered feature matrices utilized for secondary
836 analyses in R using a Seurat based pipeline [56]. Briefly, the packages Seurat v4.4.0, SeuratObject
837 v5.0.1, and SeuratWrappers v0.2.0, devtools 2.4.5, dplyr v1.1.4, harmony v1.2.0, and patchwork
838 v1.2.0, were used for analysis. Individual imported filtered feature matrices underwent filtering for
839 to only include cells with nFeatures falling between 2500-15000, nCounts lower than 200,000,
840 percent mitochondrial reads falling between 0.05-1, and percent ribosomal reads lower than 3.
841 Matrices were then merged, and individually normalized using SCTransform, regressing percent
842 mitochondrial reads, percent ribosomal reads, nFeatures, and nCounts. Integration of the data
843 was then performed on the SCT normalized data using SelectIntegrationFeatures (nFeatures =
844 4000), PrepSCTIntegration, FindIntegrationAnchors, and the IntegrateData commands.
845 Dimensional reduction using RunPCA and RunUMAP was then performed using the top 30
846 dimensions, followed by cluster analysis (FindNeighbors and FindClusters) at a resolution of 0.2.
847 Prior to subsequent analyses, where indicated, the RNA assay was normalized and scaled
848 (NormalizeData and ScaleData, and ALRA (RunALRA) mediated imputation of the data was
849 performed as previously described. Marker identification was performed using the FindAllMarkers
850 function using the ALRA assay, with a minimum fold change threshold of 0.25 and detected in a
851 minimum of 0.25 of cells.

852

853 *Pseudotime Analysis*

854 The differentiation trajectories from Seurat-identified clusters were determined using the Slingshot
855 package (version 2.6.0) in R, with unbiased selection of starting and ending points[57]. The raw
856 RNA count data and the generated Slingshot object were then utilized to run the evaluateK()
857 function, testing a range of 3 to 9 knots. The optimal number of knots was determined to be 4.
858 Subsequently, the fitGAM() function in tradeSeq (version 1.5.10) was applied using this optimal
859 value, and lineage-specific gene expression was identified through the associationTest()
860 function[58]. Heatmaps of expression changes along the lineages were created using
861 ComplexHeatmap() on log-transformed counts, and were rasterized using the "Bessel" filter in
862 ImageMagick[59]. Finally, the plotGenePseudotime() function was used to visualize raw count gene
863 expression across individual cells along the lineages derived from the Slingshot object.

864

865 *Differential Expression and GO-Term Analysis*

866 To perform differential expression between clusters, the FindMarkers function was utilized setting
867 the LogFoldChange threshold to 0.01. Significant hits were defined as having a Log2FoldChange
868 of at least 0.25 and a p-value < 0.01. GO-Term was performed using DAVID pathway analysis
869 Significant hits were then input into the Database for Annotation, Visualization
870 and Integrated Discovery (DAVID; https://david.ncifcrf.gov/home.jsp) and GO-Terms exported.
871 Significantly enriched GO-Terms were defined as GO-Terms with a p-value <0.05 after Bonferroni
872 correction.

873

874 *CellChat Analysis for sTOs*

875 Cellchat for sTO were performed using previously established methods[60,61]. Briefly, interaction
876 inputs, complex inputs, cofactor inputs, and gene info inputs were downloaded from CellChatDB
877 and cellchat objects were created using the ALRA assay. Overexpressed genes and interactions

878 were then identified using the identifyOverExpressedGenes and
879 identifyOverExpressedInteractions functions and gene expression projected onto a protein-
880 protein network using projectData. Communication probabilities were then calculated using the
881 computeCommunProb function. Communications were then filtered to include interactions
882 including a minimum of 10 cells (filtercommunication function) and probabilities calculated using
883 computeCommunProbPathway function. Aggregated networks were then calculated using
884 aggregateNet and centrality calculated using netAnalysis_computeCentrality function. Patterning
885 analysis was performed first by selecting a number of patterns using the selectK function, which
886 was assigned based on when the which Cophenetic and Silhouette values droped suddenly.
887 Pattern plots were generated using the identifyCommunicationPatterns function. Additional plots
888 were generated using standard methods as described in detailed scripts.
889

890 **Spatial Transcriptomics of Mid-Gestation Pig Placentae**

891 Tissues embedded in optimal cutting temperature (OCT) compound were sectioned at 10 μm
892 thickness and placed on a Tissue Optimization (TO) Slide to determine optimal permeabilization
893 conditions. After establishing the conditions, tissue sections were positioned within a 6.5 mm^2
894 capture area on an expression slide containing 5,000 spatially barcoded probes. The tissues were
895 subsequently fixed and stained with Hematoxylin and Eosin. Following staining, the tissues were
896 permeabilized to release mRNA, which hybridized to the spatially barcoded capture probes,
897 enabling the capture of gene expression data. Barcoded cDNA was synthesized on the slide from
898 the captured mRNA, denatured, cleaved, and transferred into a PCR tube for amplification. The
899 amplified cDNA was then used to generate standard next-generation sequencing (NGS) libraries.
900 In brief, the amplified cDNA was enzymatically fragmented, purified, and size-selected.
901 Sequencing adapters were ligated to each fragment, followed by sample index PCR. The resulting
902 libraries were sequenced on a NovaSeq6000 SP flow cell with an average of 50,000 reads per
903 probe, using a 28x10x10x90 read format.

904 **Analysis of Visium Data**

905 *QC and Cluster Analysis*

906 FASTQ files were analyzed using Spaceranger v2.1.1 using Sus scrofa genome v11.1
907 downloaded from Ensembl (www.ensembl.org). Filtered feature matrices were then utilized for
908 secondary analyses in R using a Seurat based pipeline [56]. Briefly, the packages Seurat v4.4.0,
909 SeuratObject v5.0.1, and SeuratWrappers v0.2.0, devtools 2.4.5, dplyr v1.1.4, harmony v1.2.0
910 and patchwork v1.2.0 were used for analysis. Individual imported filtered feature matrices
911 underwent filtering for to only include cells with nFeatures falling above 200 and percent ribosomal
912 reads lower than 20. Matrices were then merged, and individually normalized using SCTransform,
913 regressing percent ribosomal reads, nFeatures, and nCounts. Integration of the data was then
914 performed on the SCT normalized data using SelectIntegrationFeatures (nFeatures = 3000) and
915 remerged using Merge_Seurat_List. Variable features were then obtained using VariableFeatures
916 and dimensional reduction and cluster analysis performed using RunPCA on the top 50
917 dimensions. Cluster analysis was then perfomed using FindNeighbors (top 30 dimensions),
918 FindClusters (resolution of 0.3), and RunUMAP (top 30 dimensions). Prior to subsequent
919 analyses, where indicated, ALRA (RunALRA) mediated imputation of the data was performed as
920 previously described. Marker identification was performed using the FindAllMarkers function
921 using the ALRA assay, with a minimum fold change threshold of 0.25 and detected in a minimum
922 of 0.25 of cells.

923

924 *Probabilistic Modeling Based Identification of sTO Clusters*

925 To identify the cluster identities in sTO we utilized a previously established method to map single
926 cell data to visium spatial transcriptomics data [56,62]. Briefly, visium spatial transcriptomics data
927 were first subsetted to only include structures known to contain trophoblasts, which reduces non-
928 specific signal. Visium data were then set to the SCT data, whereas sTO single cell data were set
929 to the integrated assay. Probabilistic transfer of labels was then performed using

930 FindTransferAnchors and TransferData functions, using sTO data as a reference and subsetted
931 visium data as the query. To identify shared markers between sTO and their corresponding tissue
932 structures, marker lists for the integrated assay of sTO assay and the SCT assay of the visium
933 data were generated using FindAllMarkers with a minimum fold change threshold of 0.25 and
934 detected in a minimum of 0.25 of cells. Individual sTO clusters and their corresponding tissue
935 structure clusters were then filtered and the lists inner joined to generate shared marker lists.
936
937 *CellChat Analysis for Visium*
938 Cellchat was performed using previously established methods using the packages CellChat and
939 NMF [60,61]. Briefly, interaction inputs, complex inputs, cofactor inputs, and gene info inputs were
940 downloaded from CellChatDB and cellchat objects were created using the ALRA assay.
941 Overexpressed genes and interactions were then identified using the
942 identifyOverExpressedGenes and identifyOverExpressedInteractions functions. Communication
943 probabilities were then calculated using the computeCommunProb function. Interactions were
944 corrected for both distance and cell to cell contact, with the maximum diffusion
945 interaction/diffusion length being set to 250um and the cell spot center to spot center range being
946 set to 100um. Communications were then filtered to include interactions including a minimum of
947 10 cells (filtercommunication function) and probabilities calculated using
948 computeCommunProbPathway function. Aggregated networks were then calculated using
949 aggregateNet. Patterning analysis was performed first by selecting a number of patterns using
950 the selectK function, which was assigned based on when the which Cophenetic and Silhouette
951 values droped suddenly. Pattern plots were generated using the identifyCommunicationPatterns
952 function. Additional plots were generated using standard methods as described in detailed scripts.
953
954 **DATA AND CODE AVALIABILITY**

All code is publicly available on the Coyne Lab Github (https://github.com/CoyneLabDuke). All raw and mapped data obtained via Bulk RNA-Sequencing, Single Cell, and Visium Spatial Transcriptomics data generated in this paper are deposited on the Gene Expression Omnibus (GEO) and additionally are available via the Sequencing Read Archive (SRA). Additionally, a searchable, user-friendly version of the Visium Spatial Transcriptomics dataset has been uploaded at https://coynelab.shinyapps.io/myshinyapp/.

ACKNOWLEDGEMENTS

We would like to thank the Duke Molecular Genomics Core facility for assistance with the generation of bulk RNA-sequencing data, Single-Cell Transcriptomics data, and Visium Spatial Transcriptomics data.

FUNDING SOURCES

This work was supported by funds from Duke University (C.B.C.). Placental tissues samples were derived from work supported by the Foundational and Applied Science Program, project award no. 2023-67015-39338, from the U.S. Department of Agriculture's National Institute of Food and Agriculture.

BIBLIOGRAPHY

1. Hay, W.W., Jr. (1994). Placental transport of nutrients to the fetus. Horm Res *42*, 215-222. 10.1159/000184196.

2. Lager, S., and Powell, T.L. (2012). Regulation of nutrient transport across the placenta. J Pregnancy *2012*, 179827. 10.1155/2012/179827.

3. Tal, R., and Taylor, H.S. (2000). Endocrinology of Pregnancy. In Endotext, K.R. Feingold, B. Anawalt, M.R. Blackman, A. Boyce, G. Chrousos, E. Corpas, W.W. de Herder, K. Dhatariya, K. Dungan, J. Hofland, et al., eds.

4. Arora, N., Sadovsky, Y., Dermody, T.S., and Coyne, C.B. (2017). Microbial Vertical Transmission during Human Pregnancy. Cell Host Microbe *21*, 561-567. 10.1016/j.chom.2017.04.007.

5. Megli, C.J., and Coyne, C.B. (2022). Infections at the maternal-fetal interface: an overview of pathogenesis and defence. Nat Rev Microbiol *20*, 67-82. 10.1038/s41579-021-00610-y.

6. Roberts, R.M., Green, J.A., and Schulz, L.C. (2016). The evolution of the placenta. Reproduction *152*, R179-R189. 10.1530/Rep-16-0325.

7. Moffett, A., and Loke, C. (2006). Immunology of placentation in eutherian mammals. Nat Rev Immunol *6*, 584-594. 10.1038/nri1897.

8. Mika, K., Whittington, C.M., McAllan, B.M., and Lynch, V.J. (2022). Gene expression phylogenies and ancestral transcriptome reconstruction resolves major transitions in the origins of pregnancy. Elife *11*. 10.7554/eLife.74297.

9. Carter, A.M. (2012). Evolution of Placental Function in Mammals: The Molecular Basis of Gas and Nutrient Transfer, Hormone Secretion, and Immune Responses. Physiol Rev *92*, 1543-1576. 10.1152/physrev.00040.2011.

10. Chen, Y., Siriwardena, D., Penfold, C., Pavlinek, A., and Boroviak, T.E. (2022). An integrated atlas of human placental development delineates essential regulators of trophoblast stem cells. Development *149*. 10.1242/dev.200171.

11. Liu, Y., Fan, X., Wang, R., Lu, X., Dang, Y.L., Wang, H., Lin, H.Y., Zhu, C., Ge, H., Cross, J.C., and Wang, H. (2018). Single-cell RNA-seq reveals the diversity of trophoblast subtypes and patterns of differentiation in the human placenta. Cell Res *28*, 819-832. 10.1038/s41422-018-0066-y.

12. Papuchova, H., Kshirsagar, S., Xu, L., Bougleux Gomes, H.A., Li, Q., Iyer, V., Norwitz, E.R., Strominger, J.L., and Tilburgs, T. (2020). Three types of HLA-G+ extravillous trophoblasts that have distinct immune regulatory properties. Proc Natl Acad Sci U S A *117*, 15772-15777. 10.1073/pnas.2000484117.

13. Tilburgs, T., Crespo, A.C., van der Zwan, A., Rybalov, B., Raj, T., Stranger, B., Gardner, L., Moffett, A., and Strominger, J.L. (2015). Human HLA-G+ extravillous trophoblasts:

1018 Immune-activating cells that interact with decidual leukocytes. Proc Natl Acad Sci U S A
1019 *112*, 7219-7224. 10.1073/pnas.1507977112.

1020 14. Wallace, A.E., Fraser, R., and Cartwright, J.E. (2012). Extravillous trophoblast and
1021 decidual natural killer cells: a remodelling partnership. Hum Reprod Update *18*, 458-471.
1022 10.1093/humupd/dms015.

1023 15. Fuchs, R., and Ellinger, I. (2004). Endocytic and transcytotic processes in villous
1024 syncytiotrophoblast: role in nutrient transport to the human fetus. Traffic *5*, 725-738.
1025 10.1111/j.1600-0854.2004.00221.x.

1026 16. Robbins, J.R., Skrzypczynska, K.M., Zeldovich, V.B., Kapidzic, M., and Bakardjiev, A.I.
1027 (2010). Placental syncytiotrophoblast constitutes a major barrier to vertical transmission
1028 of Listeria monocytogenes. PLoS Pathog *6*, e1000732. 10.1371/journal.ppat.1000732.

1029 17. Friess, A.E., Sinowatz, F., Skolek-Winnisch, R., and Traautner, W. (1980). The placenta
1030 of the pig. I. Finestructural changes of the placental barrier during pregnancy. Anat
1031 Embryol (Berl) *158*, 179-191. 10.1007/BF00315905.

1032 18. McLendon, B.A., Kramer, A.C., Seo, H., Burghardt, R.C., Bazer, F.W., Wu, G., and
1033 Johnson, G.A. (2022). Temporal and spatial expression of aquaporins 1, 5, 8, and 9:
1034 Potential transport of water across the endometrium and chorioallantois of pigs. Placenta
1035 *124*, 28-36. 10.1016/j.placenta.2022.05.007.

1036 19. Stenhouse, C., Seo, H., Wu, G., Johnson, G.A., and Bazer, F.W. (2022). Insights into
1037 the Regulation of Implantation and Placentation in Humans, Rodents, Sheep, and Pigs.
1038 Adv Exp Med Biol *1354*, 25-48. 10.1007/978-3-030-85686-1_2.

1039 20. Friess, A.E., Sinowatz, F., Skolek-Winnisch, R., and Trautner, W. (1981). The placenta
1040 of the pig. II. The ultrastructure of the areolae. Anat Embryol (Berl) *163*, 43-53.
1041 10.1007/BF00315769.

1042 21. Roberts, R.M., Raub, T.J., and Bazer, F.W. (1986). Role of uteroferrin in transplacental
1043 iron transport in the pig. Fed Proc *45*, 2513-2518.

1044 22. Song, G., Bailey, D.W., Dunlap, K.A., Burghardt, R.C., Spencer, T.E., Bazer, F.W., and
1045 Johnson, G.A. (2010). Cathepsin B, cathepsin L, and cystatin C in the porcine uterus
1046 and placenta: potential roles in endometrial/placental remodeling and in fluid-phase
1047 transport of proteins secreted by uterine epithelia across placental areolae. Biol Reprod
1048 *82*, 854-864. 10.1095/biolreprod.109.080929.

1049 23. Jaeger, L.A., Spiegel, A.K., Ing, N.H., Johnson, G.A., Bazer, F.W., and Burghardt, R.C.
1050 (2005). Functional effects of transforming growth factor beta on adhesive properties of
1051 porcine trophectoderm. Endocrinology *146*, 3933-3942. 10.1210/en.2005-0090.

1052 24. Suleman, M., Malgarin, C.M., Detmer, S.E., Harding, J.C.S., and MacPhee, D.J. (2019).
1053 The porcine trophoblast cell line PTr2 is susceptible to porcine reproductive and
1054 respiratory syndrome virus-2 infection. Placenta *88*, 44-51.
1055 10.1016/j.placenta.2019.10.004.

1056 25. Ramsoondar, J., Christopherson, R.J., Guilbert, L.J., and Wegmann, T.G. (1993). A
1057 porcine trophoblast cell line that secretes growth factors which stimulate porcine
1058 macrophages. Biol Reprod *49*, 681-694. 10.1095/biolreprod49.4.681.

1059 26. Hou, D., Su, M., Li, X., Li, Z., Yun, T., Zhao, Y., Zhang, M., Zhao, L., Li, R., Yu, H., and
1060 Li, X. (2015). The Efficient Derivation of Trophoblast Cells from Porcine In Vitro Fertilized
1061 and Parthenogenetic Blastocysts and Culture with ROCK Inhibitor Y-27632. PLoS One
1062 *10*, e0142442. 10.1371/journal.pone.0142442.

1063 27. Kim, J., Koo, B.K., and Knoblich, J.A. (2020). Human organoids: model systems for
1064 human biology and medicine. Nat Rev Mol Cell Biol *21*, 571-584. 10.1038/s41580-020-
1065 0259-3.

1066 28. Yang, L., Liang, P., Yang, H., and Coyne, C.B. (2024). Trophoblast organoids with
1067 physiological polarity model placental structure and function. J Cell Sci *137*.
1068 10.1242/jcs.261528.

1069 29. Yang, L., Semmes, E.C., Ovies, C., Megli, C., Permar, S., Gilner, J.B., and Coyne, C.B.
1070 (2022). Innate immune signaling in trophoblast and decidua organoids defines
1071 differential antiviral defenses at the maternal-fetal interface. Elife *11*.
1072 10.7554/eLife.79794.

1073 30. Turco, M.Y., Gardner, L., Kay, R.G., Hamilton, R.S., Prater, M., Hollinshead, M.S.,
1074 McWhinnie, A., Esposito, L., Fernando, R., Skelton, H., et al. (2018). Trophoblast
1075 organoids as a model for maternal-fetal interactions during human placentation. Nature
1076 *564*, 263-267. 10.1038/s41586-018-0753-3.

1077 31. Keenen, M.M., Yang, L., Liang, H., Farmer, V.J., Singh, R., Gladfelter, A.S., and Coyne,
1078 C.B. (2024). Comparative analysis of the syncytiotrophoblast in placenta tissue and
1079 trophoblast organoids using snRNA sequencing. bioRxiv, 2024.2007.2001.601571.
1080 10.1101/2024.07.01.601571.

1081 32. Caldwell, A., Yang, L., Scheef, E.A., Kaur, A., and Coyne, C. (2024). Comparative
1082 analysis of rhesus macaque and human placental organoids highlights evolutionary
1083 differences in placentation. bioRxiv, 2024.2010.2011.617873.
1084 10.1101/2024.10.11.617873.

1085 33. Guidoni, P.B., Pasternak, J.A., Hamonic, G., MacPhee, D.J., and Harding, J.C.S. (2021).
1086 Decreased tight junction protein intensity in the placenta of porcine reproductive and
1087 respiratory syndrome virus-2 infected fetuses. Placenta *112*, 153-161.
1088 10.1016/j.placenta.2021.07.300.

1089 34. Teixeira, S.A., Ibelli, A.M.G., Cantao, M.E., Oliveira, H.C., Ledur, M.C., Peixoto, J.O.,
1090 Marques, D.B.D., Costa, K.A., Coutinho, L.L., and Guimaraes, S.E.F. (2019). Sex
1091 Determination Using RNA-Sequencing Analyses in Early Prenatal Pig Development.
1092 Genes (Basel) *10*. 10.3390/genes10121010.

1093 35. Kramer, A.C., Steinhauser, C.B., Gao, H.J., Seo, H., McLendon, B.A., Burghardt, R.C.,
1094 Wu, G.Y., Bazer, F.W., and Johnson, G.A. (2020). Steroids Regulate SLC2A1 and
1095 SLC2A3 to Deliver Glucose Into Trophectoderm for Metabolism via Glycolysis.
1096 Endocrinology *161*. ARTN bqaa098

10.1210/endocr/bqaa098.

36. Kramer, A.C., Jansson, T., Bale, T.L., and Powell, T.L. (2023). Maternal-fetal cross-talk via the placenta: influence on offspring development and metabolism. Development *150*. 10.1242/dev.202088.

37. Lakhal-Littleton, S. (2021). Advances in understanding the crosstalk between mother and fetus on iron utilization. Semin Hematol *58*, 153-160. 10.1053/j.seminhematol.2021.06.003.

38. Lash, G.E. (2015). Molecular Cross-Talk at the Feto-Maternal Interface. Cold Spring Harb Perspect Med *5*. 10.1101/cshperspect.a023010.

39. Tian, Q., He, J.P., Zhu, C., Zhu, Q.Y., Li, Y.G., and Liu, J.L. (2022). Revisiting the Transcriptome Landscape of Pig Embryo Implantation Site at Single-Cell Resolution. Frontiers in Cell and Developmental Biology *10*. ARTN 796358 10.3389/fcell.2022.796358.

40. Zang, X.P., Gu, S.C., Wang, W.J., Shi, J.S., Gan, J.Y., Hu, Q., Zhou, C., Ding, Y., He, Y.J., Jiang, L., et al. (2024). Dynamic intrauterine crosstalk promotes porcine embryo implantation during early pregnancy. Sci China Life Sci *67*, 1676-1696. 10.1007/s11427-023-2557-x.

41. Cook, H.a.S.L. (2024). The United States Pork Industry 2023: Current Structure and Economic Importance. National Pork Producers Council. https://nppc.org/wp-content/uploads/2024/06/U.S.-Economic-Contribution-Report-6.28.24.pdf.

42. Bingying Liu, S.R., Hong An, Yixuan Liang, Xihui Sheng, Xiaolong Qi, Longfei Xiao, Xiangguo Wang (2024). Establishment of functional trophoblast organoids from trophoblast cells of bovine placenta. Cells & Development *Volume 180*. https://doi.org/10.1016/j.cdev.2024.203970.

43. Knight, J.W., Bazer, F.W., Thatcher, W.W., Franke, D.E., and Wallace, H.D. (1977). Conceptus Development in Intact and Unilaterally Hysterectomized-Ovariectomized Gilts - Interrelations among Hormonal Status, Placental Development, Fetal Fluids and Fetal Growth. J Anim Sci *44*, 620-637. DOI 10.2527/jas1977.444620x.

44. Amoroso, E.C., Hancock, N.A., Kellas, L. (1958). The Foetal Membranes and Placenta of the Hippopotamus (Hippopotamus amphibius (Linnaeus)). Proceedings of the Zoological Society of London *130*, 437-447.

45. Jones, C.J.P., Aplin, J.D., Salbany, A.C., Allen, W.R., and Wilsher, S. (2022). Observations on the glycosylation of the term placenta of the Indo-Pacific Bottlenose Dolphin ( ): A lectin histochemical study. Placenta *124*, 37-43. 10.1016/j.placenta.2022.05.013.

46. Iturrizaga, D.M., Verechia, F.T., Santos, T.C., Bombonato, P.P., Teixeira, D.G., and Miglino, M.A. (2007). The materno-fetal interface in llama ( ). Pesqui Vet Brasil *27*, 221-228. Doi 10.1590/S0100-736x2007000600001.

1135 47. Frank, J.W., Li, X.L., Erikson, D.W., Wu, G.Y., Bazer, F.W., Bayless, K.J., Burghardt,
1136 R.C., and Johnson, G.A. (2010). Expression of SPP1 (Osteopontin) and the Aggregation
1137 of Integrins into Focal Adhesions Is an Adaptation to Mechanical Forces at the Uterine-
1138 Placental Interface in Pigs. Biology of Reproduction, 147-147.

1139 48. Keenen, M.M., Yang, L., Liang, H., Farmer, V.J., Singh, R., Gladfelter, A.S., and Coyne,
1140 C.B. (2024). Comparative analysis of the syncytiotrophoblast in placenta tissue and
1141 trophoblast organoids using snRNA sequencing. bioRxiv. 10.1101/2024.07.01.601571.

1142 49. Mitsiadis, T.A., Salmivirta, M., Muramatsu, T., Muramatsu, H., Rauvala, H., Lehtonen,
1143 E., Jalkanen, M., and Thesleff, I. (1995). Expression of the heparin-binding cytokines,
1144 midkine (MK) and HB-GAM (pleiotrophin) is associated with epithelial-mesenchymal
1145 interactions during fetal development and organogenesis. Development *121*, 37-51.
1146 10.1242/dev.121.1.37.

1147 50. Satoh, J., Muramatsu, H., Moretto, G., Muramatsu, T., Chang, H.J., Kim, S.T., Cho, J.M.,
1148 and Kim, S.U. (1993). Midkine that promotes survival of fetal human neurons is
1149 produced by fetal human astrocytes in culture. Brain Res Dev Brain Res *75*, 201-205.
1150 10.1016/0165-3806(93)90024-5.

1151 51. Qin, J., Diaz-Cueto, L., Schwarze, J.E., Takahashi, Y., Imai, M., Isuzugawa, K.,
1152 Yamamoto, S., Chang, K.T., Gerton, G.L., and Imakawa, K. (2005). Effects of
1153 progranulin on blastocyst hatching and subsequent adhesion and outgrowth in the
1154 mouse. Biol Reprod *73*, 434-442. 10.1095/biolreprod.105.040030.

1155 52. Toh, H., Cao, M., Daniels, E., and Bateman, A. (2013). Expression of the growth factor
1156 progranulin in endothelial cells influences growth and development of blood vessels: a
1157 novel mouse model. PLoS One *8*, e64989. 10.1371/journal.pone.0064989.

1158 53. Xu, B., Chen, X., Ding, Y., Chen, C., Liu, T., and Zhang, H. (2020). Abnormal
1159 angiogenesis of placenta in progranulin-deficient mice. Mol Med Rep *22*, 3482-3492.
1160 10.3892/mmr.2020.11438.

1161 54. Wei, Q.Q., Li, R.Q., Zhong, L., Mu, H.Y., Zhang, S.P., Yue, L., Xiang, J.Z., Li, E.H., Zhi,
1162 M.L., Cao, S.Y., and Han, J.Y. (2018). Lineage specification revealed by single-cell gene
1163 expression analysis in porcine preimplantation embryos. Biology of Reproduction *99*,
1164 283-292. 10.1093/biolre/ioy062.

1165 55. Ison, E.K., Kent-Dennis, C.E., Fazioli, J., Mulligan, M.K., Pham, A., and Pasternak, J.A.
1166 (2023). Compensatory mechanisms in response to induced hypothyroidism in the late
1167 gestation pig fetus. Biology of Reproduction *108*, 731-743. 10.1093/biolre/ioad024.

1168 56. Hao, Y., Hao, S., Andersen-Nissen, E., Mauck, W.M., 3rd, Zheng, S., Butler, A., Lee,
1169 M.J., Wilk, A.J., Darby, C., Zager, M., et al. (2021). Integrated analysis of multimodal
1170 single-cell data. Cell *184*, 3573-3587 e3529. 10.1016/j.cell.2021.04.048.

1171 57. Street, K., Risso, D., Fletcher, R.B., Das, D., Ngai, J., Yosef, N., Purdom, E., and Dudoit,
1172 S. (2018). Slingshot: cell lineage and pseudotime inference for single-cell
1173 transcriptomics. BMC Genomics *19*, 477. 10.1186/s12864-018-4772-0.

58. Van den Berge, K., Roux de Bezieux, H., Street, K., Saelens, W., Cannoodt, R., Saeys, Y., Dudoit, S., and Clement, L. (2020). Trajectory-based differential expression analysis for single-cell sequencing data. Nat Commun *11*, 1201. 10.1038/s41467-020-14766-3.

59. Ooms, J. (2023). magick: Advanced Graphics and Image-Processing in R.

60. Jin, S., Guerrero-Juarez, C.F., Zhang, L., Chang, I., Ramos, R., Kuan, C.H., Myung, P., Plikus, M.V., and Nie, Q. (2021). Inference and analysis of cell-cell communication using CellChat. Nat Commun *12*, 1088. 10.1038/s41467-021-21246-9.

61. Jin, S., Plikus, M.V., and Nie, Q. (2024). CellChat for systematic analysis of cell-cell communication from single-cell transcriptomics. Nat Protoc. 10.1038/s41596-024-01045-4.

62. Stuart, T., Butler, A., Hoffman, P., Hafemeister, C., Papalexi, E., Mauck, W.M., 3rd, Hao, Y., Stoeckius, M., Smibert, P., and Satija, R. (2019). Comprehensive Integration of Single-Cell Data. Cell *177*, 1888-1902 e1821. 10.1016/j.cell.2019.05.031.